J. Fluid Mech. (2017), *vol.* 826, *pp.* 302–334.
doi:10.1017/jfm.2017.422

Topology of three-dimensional steady cellular flow in a two-sided anti-parallel lid-driven cavity

Francesco Romanò[1,†], Stefan Albensoeder[2] and Hendrik C. Kuhlmann[1]

[1]Institute of Fluid Mechanics and Heat Transfer, TU Wien, Getreidemarkt 9, 1060 Vienna, Austria
[2]School of Mathematics and Science, Carl von Ossietzky Universität, 26111 Oldenburg, Germany

(Received 6 July 2016; revised 22 April 2017; accepted 13 June 2017;
first published online 3 August 2017)

The structure of the incompressible steady three-dimensional flow in a two-sided anti-symmetrically lid-driven cavity is investigated for an aspect ratio $\Gamma = 1.7$ and spanwise-periodic boundary conditions. Flow fields are computed by solving the Navier–Stokes equations with a fully spectral method on 128^3 grid points utilizing second-order asymptotic solutions near the singular corners. The supercritical flow arises in the form of steady rectangular convection cells within which the flow is point symmetric with respect to the cell centre. Global streamline chaos occupying the whole domain is found immediately above the threshold to three-dimensional flow. Beyond a certain Reynolds number the chaotic sea recedes from the interior, giving way to regular islands. The regular Kolmogorov–Arnold–Moser tori grow with increasing Reynolds number before they shrink again to eventually vanish completely. The global chaos at onset is traced back to the existence of one hyperbolic and two elliptic periodic lines in the basic flow. The singular points of the three-dimensional flow which emerge from the periodic lines quickly change such that, for a wide range of supercritical Reynolds number, each periodic convection cell houses a double spiralling-in saddle focus in its centre, a spiralling-out saddle focus on each of the two cell boundaries and two types of saddle limit cycle on the walls. A representative analysis for $Re = 500$ shows chaotic streamlines to be due to chaotic tangling of the two-dimensional stable manifold of the central spiralling-in saddle focus and the two-dimensional unstable manifold of the central wall limit cycle. Embedded Kolmogorov–Arnold–Moser tori and the associated closed streamlines are computed for several supercritical Reynolds numbers owing to their importance for particle transport.

Key words: chaotic advection, nonlinear dynamical systems, topological fluid dynamics

1. Introduction

The flow of an incompressible Newtonian fluid in a lid-driven cavity is a classical problem in fluid mechanics, first pioneered analytically and numerically by Burggraf (1966). The system is also an important model for environmental and industrial flows

† Email address for correspondence: francesco.romano@tuwien.ac.at

(Freitas & Street 1988; Iwatsu *et al.* 1989; Shankar & Deshpande 2000). Cavity flows have been considered in chemical engineering (Aidun, Triantafillopoulos & Benson 1991; Benjamin, Anderson & Scriven 1995) and to model condensation dryers (Alleborn, Raszillier & Durst 1999), polymer melts and coating processes (Gaskell *et al.* 1996, 1998). Other applications relate to metal casting and galvanization. The related problem of compressible flow in a shear-driven cavity is of interest in aeronautical applications if, e.g. airframe noise is to be reduced (see, e.g. Crighton 1991).

Owing to the simplicity of the geometry and boundary conditions the lid-driven cavity problem is frequently employed as a numerical benchmark (Ghia, Ghia & Shin 1982; Schreiber & Keller 1983; Albensoeder & Kuhlmann 2005; Bruneau & Saad 2006). It is also interesting for fundamental fluid mechanics, since this type of separated flow exhibits a rich variety of characteristics such as the evolution of a vortex core to solid-body rotation at high Reynolds number in two-dimensional flow (Batchelor 1956) or viscous corner eddies (Moffatt 1964). Other interesting features are the multiplicity of steady two-dimensional flows (Albensoeder, Kuhlmann & Rath 2001*a*) and a wealth of different hydrodynamic instabilities (Albensoeder & Kuhlmann 2003) ranging from centrifugal (Ramanan & Homsy 1994; Albensoeder, Kuhlmann & Rath 2001*b*) to elliptic mechanisms (Albensoeder & Kuhlmann 2002). As a result the lid-driven cavity has evolved to a paradigm for vortex flows in confined geometries. A review covering many of these aspects is due to Shankar & Deshpande (2000).

The present investigation is concerned with the streamline topology in a rectangular cavity in which the flow is driven by the steady anti-parallel motion of two facing walls. The streamline topology in a similar cavity has been considered before in the context of mixing at low Reynolds number and under time-dependent forcing (see e.g. Ottino 1989). Here, we investigate the existence, properties and evolution of three-dimensional steady flow structures at much larger Reynolds numbers. Of interest is the organization of the flow around the singular points which change in number and character when the Reynolds number increases and the flow becomes three-dimensional. The structure of the regions of regular and chaotic streamlines is not only important for mixing, but also plays a crucial role for the transport and accumulation of finite-size suspended particles (Hofmann & Kuhlmann 2011; Mukin & Kuhlmann 2013; Muldoon & Kuhlmann 2016).

The theoretical backbone of chaotic mixing is the local Hamiltonian structure of incompressible three-dimensional solutions of the Navier–Stokes equations. As shown by Bajer (1994), the classical theory and analysis tools developed for Hamiltonian systems can be extended to three-dimensional steady fluid flows when interpreting these locally as Hamiltonian systems with 1.5 degrees of freedom. As pointed out by Aref (1984) and Aref (1990) the theory of chaotic advection based on this analogy is of considerable importance for the understanding of the fluid dynamics, mixing and de-mixing and corresponding applications, even in laminar flows and for very low Reynolds numbers (see e.g. Ottino 1989, 1990; Boyland, Aref & Stremler 2000; Ottino & Khakhar 2000).

Initial studies on streamline topology focusing on mixing were carried out for low Reynolds number flow in two-dimensional configurations in which the forcing was time dependent. Chien, Rising & Ottino (1986) and Leong & Ottino (1989) experimentally investigated the two-dimensional Stokes flow ($Re = O(1)$) in a cavity driven by two facing lids which move according to a certain temporal protocol including continuous and discontinuous motion. A rich behaviour in terms of periodic

points and regular islands was found. They experimentally demonstrated that chaotic mixing can be achieved in boundary-driven Stokes flows via time-periodic driving. Their studies were extended numerically by Anderson *et al.* (2000) who included the effect of inertia ($Re = 50$) on the mixing process in two-dimensional Navier–Stokes flows driven by a superposition of a constant and a time-harmonic forcing. They have shown that, even though regular and chaotic regions of the flow do not mix, the presence of Kolmogorov–Arnold–Moser tori might be used to enhance the effective mixing of the flow. Hwang, Anderson & Hulsen (2005) and Pai, Prakash & Patnaik (2013) numerically investigated the effect of freely suspended particles and passive inserts on chaotic mixing in two-dimensional Stokes flow inside a lid-driven square cavity, while Xu & Gilchrist (2010) studied the mixing efficiency of particles in the presence of shear-induced particle migration. An important achievement of these investigations consists of showing protocols for an efficient mixing of fluids at small scales do not well perform for suspensions.

Since a Lagrangian description of three-dimensional steady incompressible Navier–Stokes flows is computationally very expensive, most numerical investigations of the topology of Navier–Stokes flows have been concerned with linear or nonlinear time-dependent two-dimensional flows for which a marching technique can be employed. Oteski *et al.* (2015) and Contreras, de la Cruz & Ramos (2016) were concerned with differentially heated cavity flows. In a two-dimensional set-up Oteski *et al.* (2015) identified a route to chaos which brings the flow from steadiness to hyperchaotic states as the Rayleigh number increases. They interpreted such a scenario as a frequency locking mechanism, typical of Arnold tongues. Contreras *et al.* (2016) focused on a Stokesian flow in a three-dimensional cubic container with time-dependent boundary conditions. They demonstrated the existence of invariant surfaces with spheroidal character and classified the dynamics on these invariant surfaces which shows a behaviour similar to bifurcations of fixed points of area-preserving maps. Other work has dealt with closed-form solutions of the Navier–Stokes or Euler equations such as the ABC flow (see, e.g. Dombre *et al.* 1986; Haller 2001) or with Stokes flow for which the superposition principle can be employed. Kroujiline & Stone (1999), for instance, numerically and analytically investigated the onset of chaotic motion in Stokes flow in a spherical drop due to perturbations of axisymmetry. They used area-preserving whisker maps to estimate the width of the chaotic layer which was found to form about the separatrix of the unperturbed flow. Arter (1983) considered bimodal convection in the Rayleigh–Bénard problem slightly above the convective threshold. He demonstrated that the presence of higher-order terms in an expansion of the weakly nonlinear flow causes chaotic streamlines to invade the region of regular motion from the boundaries of the convection cells (see also Chernikov & Schmidt 1992). For another paradigmatic system, the Taylor–Couette problem, a similar behaviour was found by Broomhead & Ryrie (1988) within an analytical model for wavy Taylor vortices. Upon the onset of waviness chaotic layers are established around the separatrices between the Taylor vortices. The reason for this behaviour is the breakup of the heteroclinic connection of two hyperbolic points on the cylindrical walls which are connected by the separating streamline in the unperturbed axisymmetric steady flow. Rudman (1998) numerically investigated particle dispersion in wavy Taylor–Couette flow, confirming the results of Broomhead & Ryrie (1988). They found, moreover, that the structure of the particle dispersion strongly depends on the flow state with the possibility of heavy particles being trapped in the vortex cores. The gradual invasion of the chaotic region from the boundaries seems to be a generic feature when a two-dimensional flow becomes

time dependent or three-dimensional. According to Biemond *et al.* (2008) heteroclinic orbits which exist in two-dimensional steady flow break into heteroclinic tangles upon the onset of time dependence. Since these heteroclinic connections frequently involve separation and/or reattachment points, the flow becomes ergodic from the boundaries.

There are only very few investigations of the streamline topology of fully three-dimensional steady or time-dependent Navier–Stokes flows. Ishii, Ota & Adachi (2012) were among the first to numerically demonstrate Lagrangian transport in the three-dimensional steady flow in single-lid-driven cavities for different aspect ratios (see also Ishii & Iwatsu 1990; Ishii & Adachi 2006). For Reynolds numbers in the range $Re \in [100, 400]$ different Kolmogorov–Arnold–Moser (KAM) tori embedded in a chaotic flow have been identified. Mukin & Kuhlmann (2013) considered a three-dimensional hydrothermal wave in a liquid bridge which is driven by thermocapillary surface stresses. In this type of flow certain KAM tori can be extremely compressed towards the free surface, a topological property which was shown to have a profound influence on the transport and de-mixing of suspended particles. Sotiropoulos, Ventikos & Lackey (2001) have identified a mechanism causing chaotic transport in steady three-dimensional vortex-breakdown bubbles computed numerically (Sotiropoulos & Ventikos 2001). The appearance of chaotic regions was traced back to Shilnikov's mechanism (Shilnikov 1965) which relies on a homoclinic orbit of an inward-spiralling saddle focus. Exponentially small three-dimensional perturbations, present in every experiment, of the vortex-breakdown bubble can trigger chaotic streamlines. As a result chaotic streamlines gradually invade the bulk of the breakdown bubble from the perturbed surface of separation.

In the present paper we investigate the laminar, incompressible flow in a cavity driven by two facing side walls which move steadily in opposite directions and which is periodically extended in the third (spanwise) dimension. The system has received considerable attention (see e.g. Tiwari & Das 2007) and it exhibits different three-dimensional flow instabilities (see, e.g. Kuhlmann, Wanschura & Rath 1997; Albensoeder & Kuhlmann 2002; Blohm & Kuhlmann 2002). For a separation of the moving walls which is $\Gamma = 1.7$ times the height of the cavity the basic two-dimensional flow exhibits three singular points, one hyperbolic and two elliptic ones, defining a cat's-eye flow. We are interested in the evolution of these fixed points as the Reynolds number is increased beyond the onset of three-dimensional flow which arises in form of steady periodic prismatic cells (Albensoeder *et al.* 2001*b*) due to an elliptic instability mechanism (Bayly 1986; Pierrehumbert 1986; Waleffe 1990). The singular points are expected to have a significant effect on the organization of chaos in the system as a function of the Reynolds number. The detailed streamline topology is of interest and decisive importance for the transport of suspended particles and, in particular, for a rapid accumulation mechanism which has only been observed recently (Kuhlmann *et al.* 2016) and which depends on the particle size. With this motivation in mind and based on accurate numerical solutions of the Navier–Stokes equations the cellular flow is investigated with respect to its topological properties including singular points and regular versus chaotic motion.

Section 2 presents the mathematical formulation of the problem under investigation. In § 3 the numerical method employed to simulate the three-dimensional flow is discussed along with the algorithm to compute the streamlines. Results are presented and discussed in § 4. Section 5 is dedicated to a discussion and conclusions.

2. Problem formulation

A closed cavity of rectangular cross-section occupied by an incompressible Newtonian fluid of constant density ρ and kinematic viscosity ν is considered.

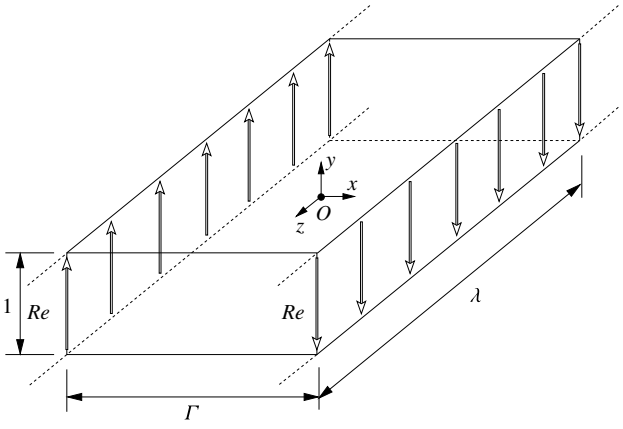

FIGURE 1. Sketch of the two-sided anti-parallel lid-driven cavity. The coordinate origin O is located in the cavity centre (dot). The cavity width Γ and the period λ are given in units of the cavity height H.

The geometry in the (x, y)-plane is defined by the height H in y-direction and the width D in x-direction. In the z-direction the cavity is assumed to be infinitely extended. The flow is driven by two facing parallel side walls at $x = \pm D/2$ which move with constant velocity U in opposite y-directions.

Following Albensoeder & Kuhlmann (2002) the viscous scaling

$$\hat{\boldsymbol{u}} = \boldsymbol{u}\frac{\nu}{H}, \quad \hat{\boldsymbol{x}} = \boldsymbol{x}H, \quad \hat{t} = t\frac{H^2}{\nu}, \quad \hat{p} = p\frac{\rho\nu^2}{H^2} \tag{2.1a–d}$$

is adopted, where $\boldsymbol{u}$ and p are the velocity and pressure fields, respectively, $\boldsymbol{x} = (x, y, z)$ and t are spatial and temporal coordinates and the caret ($\hat{}$) represents dimensional quantities. The non-dimensional Navier–Stokes equations are

$$(\partial_t + \boldsymbol{u}\cdot\boldsymbol{\nabla})\boldsymbol{u} = -\boldsymbol{\nabla}p + \nabla^2\boldsymbol{u}, \tag{2.2a}$$

$$\boldsymbol{\nabla}\cdot\boldsymbol{u} = 0. \tag{2.2b}$$

The mathematical problem is closed by no-penetration and no-slip boundary conditions along the walls and by assuming periodic boundary conditions in z-direction with period λ

$$\boldsymbol{u}(y = \pm 1/2) = \boldsymbol{0}, \quad \boldsymbol{u}(x = \pm\Gamma/2) = \mp Re\,\boldsymbol{e}_y, \quad \boldsymbol{u}(z = \lambda/2) = \boldsymbol{u}(z = -\lambda/2), \tag{2.3a–c}$$

where

$$Re = \frac{UH}{\nu} \quad \text{and} \quad \Gamma = \frac{D}{H} \tag{2.4a,b}$$

are the Reynolds number and the cross-sectional aspect ratio, respectively (figure 1).

For the present investigation we consider the aspect ratio $\Gamma = 1.7$. The period in z-direction is selected to be the critical wavelength $\lambda = \lambda_c = 2.73$; for the critical curves $Re_c(\Gamma)$ and $\lambda_c(\Gamma) = 2\pi/k_c(\Gamma)$ the reader is referred to Albensoeder & Kuhlmann (2002). The aspect ratio is selected, because the critical Reynolds number $Re_c = 211.53$ is relatively small and close to its minimum at $\Gamma = 1.428$, yet the

flow at criticality exhibits the strain-dominated cat's-eye flow structure, a condition which arises in the interval $\Gamma \in [1.58, 2.066]$ (Albensoeder & Kuhlmann 2002). Since the critical mode does not change in this range of Γ, results obtained for $\Gamma = 1.7$ can be considered representative for the full range $\Gamma \in [1.58, 2.066]$. Similarly, the wavelength $\lambda = \lambda_c$ can be considered representative, because the wavelength λ_c is typically located approximately in the centre of the band of Eckhaus-stable periodic solutions; see e.g. Dominguez-Lerma, Cannell & Ahlers (1986), Riecke & Paap (1986) for Taylor vortex flow and Albensoeder & Kuhlmann (2006) for lid-driven cavity flow. Moreover, with $\lambda = \lambda_c$ the full range of finite-amplitude periodic flows can be covered from Re_c to the Reynolds number at which the flow becomes time dependent.

In the following, steady cellular flows are computed for different Reynolds numbers and they are analysed with respect to their Lagrangian properties.

3. Numerical methods

3.1. *Fluid flow*

Numerical simulations are carried out using a spectral method based on collocation (see, e.g. Canuto *et al.* 1988; Botella & Peyret 2001; Peyret 2013). In order to avoid parasite pressures of numerical origin the functional spaces to represent the discrete pressure and velocity are chosen according to the $\mathcal{P}_N$–$\mathcal{P}_{N-2}$ method.

In x- and y-directions Chebyshev–Gauss–Lobatto points are employed, whereas Fourier modes are used in z-direction which automatically guarantees a correct implementation of the periodic boundary conditions. The time discretization is accomplished by the second-order Adam–Bashforth backward Euler scheme, as in Botella (1998). The algorithm consists of a prediction step solving for an intermediate flow field $\bar{\boldsymbol{u}}$, followed by a projection onto an algebraically solenoidal velocity space

$$\frac{3\bar{\boldsymbol{u}}^{n+1} - 4\boldsymbol{u}^n + \boldsymbol{u}^{n-1}}{2\Delta t} - \nabla^2\bar{\boldsymbol{u}}^{n+1} + \boldsymbol{\nabla} p^n + 2\boldsymbol{u}^n \cdot \boldsymbol{\nabla}\boldsymbol{u}^n - \boldsymbol{u}^{n-1} \cdot \boldsymbol{\nabla}\boldsymbol{u}^{n-1} = \boldsymbol{0}, \tag{3.1a}$$

$$\bar{\boldsymbol{u}}^{n+1}|_{\partial V} = \boldsymbol{g}^{n+1}, \tag{3.1b}$$

$$\frac{3}{2}\frac{\boldsymbol{u}^{n+1} - \bar{\boldsymbol{u}}^{n+1}}{\Delta t} + \boldsymbol{\nabla}(p^{n+1} - p^n) = \boldsymbol{0}, \tag{3.1c}$$

$$\boldsymbol{\nabla} \cdot \boldsymbol{u}^{n+1} = 0, \tag{3.1d}$$

$$\boldsymbol{u}^{n+1} \cdot \boldsymbol{n}|_{\partial V} = \boldsymbol{g}^{n+1} \cdot \boldsymbol{n}, \tag{3.1e}$$

where $|_{\partial V}$ denotes the boundary of the domain V, $\boldsymbol{g}$ is the prescribed boundary velocity according to (2.3), the superscript n refers to the time step and the overbar ($\bar{}$) indicates the intermediate solution of each complete projection step. Only the first time step is reduced to first order by setting $\boldsymbol{u}^{-1} = \boldsymbol{u}^0$, $p^0 = 0$ and by replacing Δt with $3\Delta t/2$. The Uzawa method (Peyret 2013) is applied to (3.1*c*)–(3.1*e*) and the method of Phillips & Roberts (1993) is adopted to filter the singularity in the pressure owing to the absence of boundary conditions for p.

Following Botella & Peyret (1998) and Albensoeder & Kuhlmann (2005) the strength of the singularity at each of the four cross-sectional corners (edges in three dimensions) is significantly reduced by employing the second-order asymptotic solution for a single infinite wedge. Subtracting from the velocity and pressure fields a superposition of the four asymptotic solutions (suitably weighted not to induce

additional singularities) the numerical error is reduced to $O(N^{-5})$, where N is the number of modes per spatial direction used in the discretization.

All simulations are conducted with $N = 128$ modes in each space direction. Further details about the spectral method and the corner singularities were presented in Albensoeder & Kuhlmann (2005), where the verification and accuracy of the flow solver are thoroughly discussed. The simulations are continued from the initial conditions until a steady state was reached. The flow was considered a sufficiently accurate approximation to the steady state after the termination criterion (as in Albensoeder & Kuhlmann 2006)

$$\max_{x,i} \frac{|u_i(\boldsymbol{x}, t) - u_i(\boldsymbol{x}, t - \Delta t)|}{\Delta t |Re|} \leqslant 10^{-7} \tag{3.2}$$

was satisfied.

3.2. *Streamlines*

To study the topology of the three-dimensional cellular flow and its properties a Lagrangian representation of the fluid kinematics is employed. With $\boldsymbol{X}$ denoting the position of an infinitesimal fluid element with initial condition $\boldsymbol{X}_0 = \boldsymbol{X}(t = 0)$, its motion is governed by

$$\frac{\mathrm{d}\boldsymbol{X}}{\mathrm{d}t} = \boldsymbol{u}(\boldsymbol{X}). \tag{3.3}$$

Two main approximations are made in calculating the trajectory of a fluid element, i.e. its streamline. The first approximation consists in integrating (3.3) numerically. A Runge–Kutta Dormand–Prince method is employed (for details, see Dormand & Prince 1980). The method is explicit and computes fourth- and fifth-order solutions, estimates the error by the difference between both solutions, and carries on with the integration using the fifth-order solution. An adaptive time step Δt is employed such that the estimated absolute and relative errors are always less than 10^{-10}.

The second approximation in solving (3.3) is introduced by changing from an Eulerian frame of reference for computing the flow field to a Lagrangian frame of reference to compute the motion of a fluid element. To pass from the former (with a discrete spatial representation of the solution) to the latter continuous space variables are introduced which requires an interpolation of the flow field $\boldsymbol{u}$ in space to solve (3.3) by integration in time. The reader is referred to § A.1 for a detailed discussion of the interpolation and the error introduced by this approximation. All the results presented below are obtained using a spectral interpolation. The only exception concerns the calculation of Poincaré points belonging to the chaotic sea, which are computed employing a tri-linear interpolation for computational economy. For the computation of trajectories which depend very sensitively on the initial conditions a higher accuracy is obtained by using the algorithm proposed by Berrut & Trefethen (2004).

4. Results

4.1. *Symmetries and fixed points for slightly supercritical flow*

Owing to the boundary conditions a basic flow exists which is point symmetric in the (x, y)-plane and translational invariant in z. For aspect ratios $\Gamma < 1.58$ the basic flow at the critical threshold arises as a vortex with elliptic streamlines at the centre

$\lambda^e_{1,2}$	$\lambda^h_{1,2}$	$\boldsymbol{v}^e_{1,2}$	$\boldsymbol{v}^h_{1,2}$
$+100.4261\mathrm{i}$	80.9995	$(0.9167, -0.2628 + 0.3010\mathrm{i}, 0)^{\mathrm{T}}$	$(0.9993, -0.0386, 0)^{\mathrm{T}}$
$-100.4261\mathrm{i}$	-80.9995	$(0.9167, -0.2628 - 0.3010\mathrm{i}, 0)^{\mathrm{T}}$	$(0.8687, -0.4953, 0)^{\mathrm{T}}$

TABLE 1. Eigenvalues and normalized eigenvectors of the velocity gradient tensor at criticality, $Re = 211.53$, evaluated at the elliptic point e located at $(x^e, y^e) = (0.3252, -0.0955)$ and at the hyperbolic point h located at $(x^h, y^h) = (0, 0)$ of the basic flow.

$(x, y) = (0, 0)$ of the cavity for which the strain rate is less than the rate of rotation (Albensoeder & Kuhlmann 2002). For the present aspect ratio $\Gamma = 1.7 > 1.58$ the strain rate in the centre is slightly larger than the rate of rotation such that the centre is a hyperbolic point h, surrounded by two elliptic points $e_{1,2}$ forming a cat's-eyes flow pattern (see figure 2*a*). The eigenvalues and eigenvectors of the two-dimensional velocity gradient tensor evaluated at both types of the fixed points are given in table 1 for $Re = Re_c = 211.53$. Streamlines of the neutrally stable flow at $Re = Re_c$ are shown in figure 2(*a*). The three fixed points of the two-dimensional flow in the (x, y)-plane (for which $\boldsymbol{u} = 0$) extend in the third (z) dimension in form of periodic lines.

Above the critical Reynolds number the translational invariance in z is broken by a critical mode in form of steady convection cells periodic in z, one period comprising of two cells (Albensoeder & Kuhlmann 2002; Blohm & Kuhlmann 2002). The flow field of the critical mode is point symmetric with respect to the centres $\boldsymbol{x}_c = (0, 0, \pm n\lambda/2)$, $n \in \mathbb{N}_0$, of each convection cell, where the origin of the coordinate system is defined in the centre of the cell $n = 0$. Furthermore, the critical mode exhibits mirror-symmetry planes at $z_n = \pm(1 + 2n)\lambda/4$ on which the spanwise velocity w vanishes. We find these point and mirror symmetries are preserved in the full finite-amplitude supercritical flow.

Due to the breaking of the translational invariance in z the periodic lines of the fixed points for the two-dimensional flow are destroyed for $Re > Re_c$. Only four types of discrete fixed points survive (the three of those placed on the cell boundary are shown in figure 3*b*). The hyperbolic points in the cell centres and on the cell boundaries preserve their hyperbolic character only for a very small range of slightly supercritical Reynolds numbers. Due to the symmetry of the flow the fixed point in the cell centre does not move with Re. The fixed points $e_{1,2}$ on the periodic lines at $Re = Re_c$ vanish for any $Re > Re_c$, except on the cell boundaries. Only on these mirror-symmetry planes the two elliptic points smoothly transform into two weak saddle foci, one spiralling inward (s') and the other spiralling outward (s_2). These four fixed points per each cell undergo further changes in a very small range of supercritical Reynolds numbers.

The time scale for the evolution of the flow diverges at the critical point (critical slowing down) and makes numerical simulations increasingly expensive. Therefore, we approximate the slightly supercritical flow by

$$\boldsymbol{u}^{lin} = \boldsymbol{u}_0 + a\sqrt{Re - Re_c}\tilde{\boldsymbol{u}}, \tag{4.1}$$

where $\boldsymbol{u}_0$ is the basic flow at criticality and $\tilde{\boldsymbol{u}}$ the critical mode obtained by a linear stability analysis (Albensoeder & Kuhlmann 2002). In this case the critical perturbation field $\tilde{\boldsymbol{u}}$ is computed using 48^3 spectral modes. From a fit (figure 4) of the amplitude of the numerically simulated nonlinear steady flow for the lowest supercritical Reynolds numbers we determine the slope factor $a = 5.6443$ when

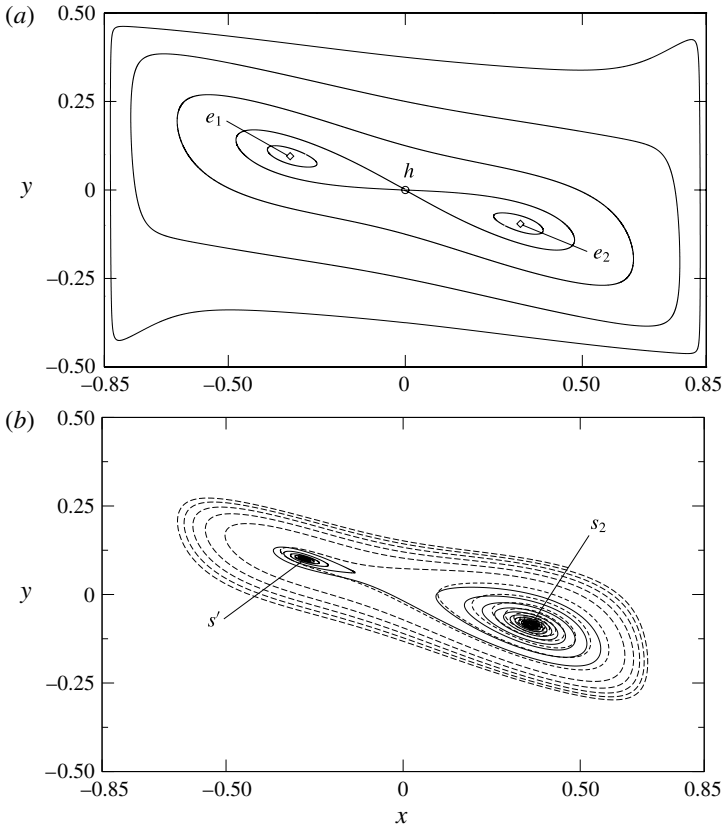

FIGURE 2. (*a*) Streamlines of the basic flow at criticality for $Re = Re_c = 211.53$ exhibiting the cat's-eye structure. The markers indicate the position of the hyperbolic and the two elliptic points. (*b*) Streamlines in the cell boundary at $z = -\lambda/4$ for slightly supercritical driving approximated by (4.1) for $Re = 1.010 \times Re_c = 213.7$ before the merging of two fixed points (full line) and for $Re = 1.0127 \times Re_C = 214.2$ after the merging (dashed line). Both streamlines spiral out of the right fixed point. The dashed streamline approaches the solid boundary, whereas the full streamline is spiralling into the left fixed point. The elliptic points $e_{1,2}$, the hyperbolic point h and the saddle foci s' and s_2 which originate from the elliptic points are labelled in the figure.

normalizing the critical mode by its maximum velocity modulus. To assess the character of the fixed point in the cell centre, denoted c, the eigenvalues of the velocity gradient tensor were calculated using (4.1). Only within a very small range of supercritical driving the fixed point c remains hyperbolic with three real eigenvalues (one positive and two being negative). Already at $\epsilon = (Re - Re_c)/Re_c = 0.0028$ the fixed point c changes from hyperbolic to an inward-spiralling saddle focus. This behaviour indicates an extreme sensitivity of the cat's-eye flow structure with respect to three-dimensional perturbations.

To investigate the behaviour of the other fixed points we computed streamlines of (4.1) on the cell boundary at $z = -\lambda/4$ on which $w = 0$. Upon the onset of the three-dimensional flow the two elliptic points change to an inward- and an outward-spiralling saddle focus. As the Reynolds number increases the inward-spiralling saddle focus, corresponding to a sink in the plane, merges with the hyperbolic point such

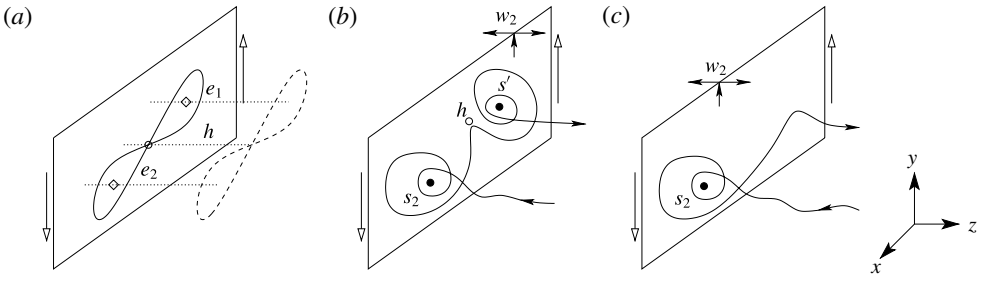

FIGURE 3. Sketch of the evolution of the fixed points and the streamline structure near a cell boundary (quadrangle) as the Reynolds number is increased from the critical value $Re = Re_c$ (a) to $Re = 1.01 \times Re_c$ (b) and $Re = 1.0127 \times Re_c$ (c). The markers show the position of elliptic points $e_{1,2}$ (◇), the hyperbolic point h (○) and the saddle foci s' and s_2 (●) which originate from the elliptic points. At $\epsilon = 0.0127$ (c) the fixed points h and s' have merged and vanished. The fixed point c in the cell centre is not shown. For $Re > Re_c$ the perimeters of the cell boundaries are degenerate saddle limit cycles $w_{1,2}$, the small arrows indicate the direction of attraction/repulsion (see 4.2).

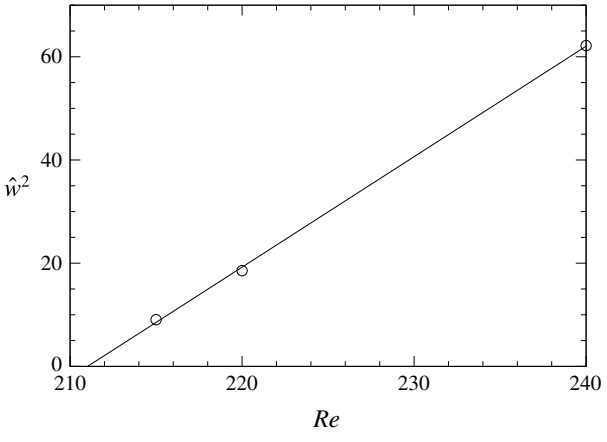

FIGURE 4. Squared amplitude of $w(x^*, y^*, z)$ along the ray $(x^*, y^*) = (-0.400687, 0)$ made by a grid line as a function of the Reynolds number.

that only the outward-spiralling saddle focus remains. We could bracket the merging point to $\epsilon \in [0.010, 0.0127]$. Streamlines on the cell boundary before and after the merging are shown in figure 2(b). The unfolding for the corresponding merger in two-dimensional incompressible flow of an elliptic with a hyperbolic point has been treated by Brøns & Hartnack (1999).

4.2. *Reynolds number dependence of the fixed points*

A representative example for the nonlinear supercritical flow field within one cell is provided in figure 5 for $Re = 500$. Projections of the velocity vectors are shown in the planes $z = -\lambda/4$ (a), $z = 0$ (b) and $y = 0$ (c). This type of cellular flow, exhibiting the same symmetries, exists for a range of aspect ratios and has been investigated experimentally by Blohm & Kuhlmann (2002) for $\Gamma = 1.96$. They found time dependence to set in at $Re \approx 825 \ldots 880$, depending on the wavelength λ.

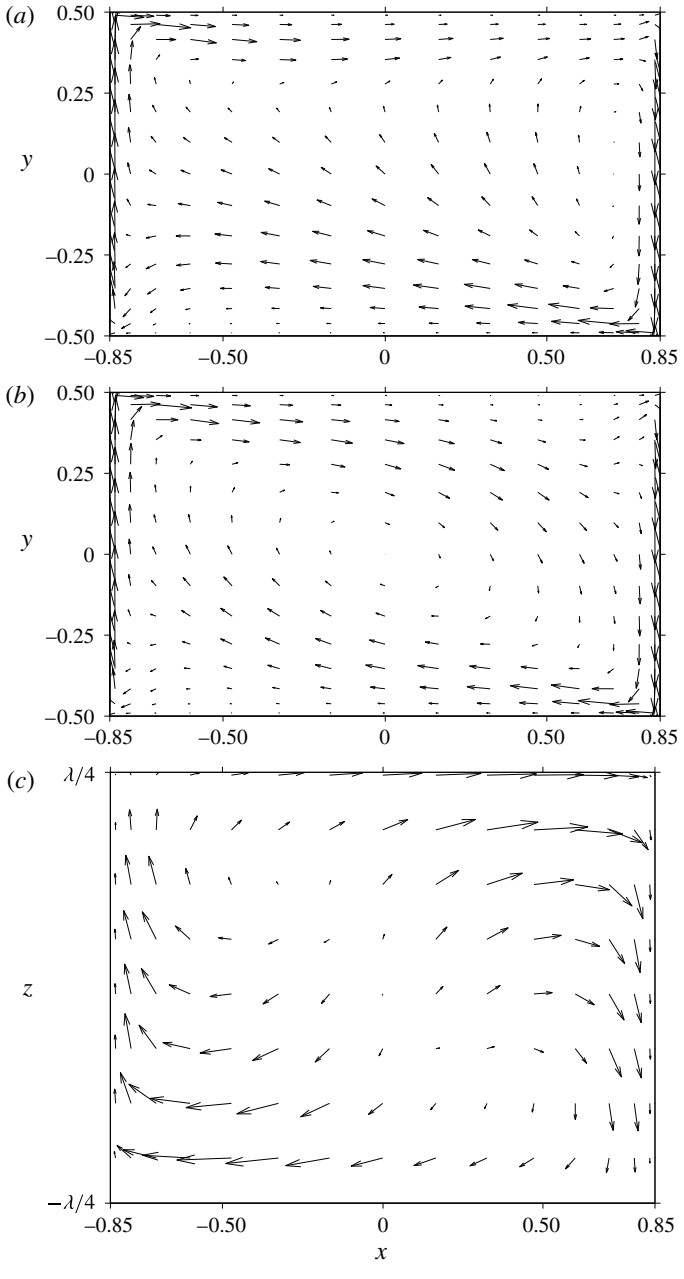

FIGURE 5. Projections of the velocity vector field for $\Gamma = 1.7$ and $Re = 500$ in the planes $(z = -\lambda/4)$ (a), $(z = 0)$ (b) and $(y = 0)$ (c). For better visualization the vectors in (a) and (b) have been magnified by a factor of 1.5 with respect to those shown in (c).

We consider the cell $n = 0$ extending from $z = -z_0 = -\lambda/4 = -0.6825$ to $z = z_0 = \lambda/4 = 0.6825$. Since the phase of the cellular pattern was not enforced in the numerical calculations, the cell boundaries z_n are accurate only up to five decimal places. Once the spiralling-in saddle focus c in the cell centre and the spiralling-out

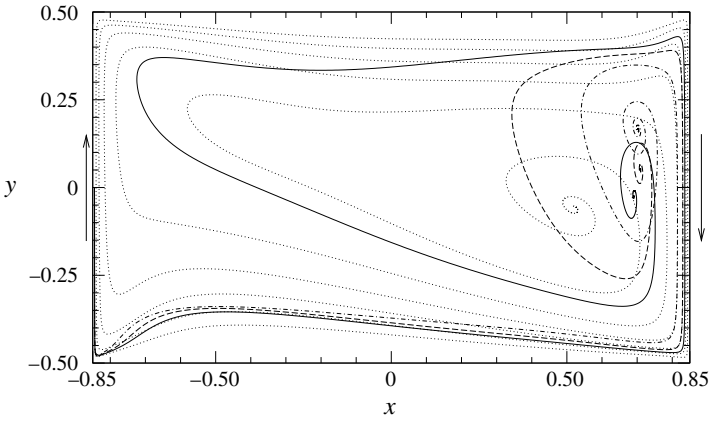

FIGURE 6. Streamlines on the cell boundary at $z = -\lambda/4$ spiralling out from the fixed point s_2 for $Re = 240$ (dotted line), $Re = 400$ (solid line), $Re = 500$ (dashed line) and $Re = 700$ (dashed-dotted line). The left boundary at $x = -\Gamma/2$ moves upward while the right boundary at $x = \Gamma/2$ moves downward.

Re	x^{vort}	y^{vort}	x^{s_2}	y^{s_2}
215	0.1288	0.0532	0.38486	−0.0872
220	0.1968	0.0797	0.42187	−0.0699
240	0.3429	0.1501	0.51758	−0.0528
275	0.4823	0.1661	0.60706	−0.0638
300	0.5740	0.1947	0.63670	−0.0645
400	0.7035	0.1778	0.69041	−0.0251
500	0.7139	0.1577	0.70915	0.0507
700	0.6857	0.1863	0.70223	0.1659

TABLE 2. Coordinates of the fixed point $\boldsymbol{x}^{s_2}$ on the cell boundary at $z = -\lambda/4$ and intersection point $\boldsymbol{x}^{vort}$ with the cell boundary at $z = -\lambda/4$ of the vortex line passing through the central fixed point c. The corresponding points on the opposite cell boundary are located anti-symmetrically.

saddle foci on each of the two cell boundaries, denoted $s_{1,2}$, are established they are robust features of the steady flow for all Reynolds numbers $Re \geqslant 215$ investigated. To find the saddle focus s_2 on the cell boundary at $z = -z_0 = -\lambda/4 = -0.6825$ a fluid element is initialized at $\boldsymbol{x} = (-0.845, 0, -\lambda/4)$ and its trajectory is integrated backward in time, enforcing $w = 0$, until the spiralling motion converges to s_2, accurate to five decimal places. Figure 6 shows the resulting streamlines on the cell boundary for different Reynolds numbers (indicated by line types). Upon an increase of the Reynolds number the fixed point s_2 moves towards the nearest moving wall (at $x = \Gamma/2$) before turning to the direction of the corner upstream of the moving wall. The coordinates of the spiralling-out saddle focus s_2 are given in table 2 as function of the Reynolds number.

To characterize the fixed points c and s_2 the eigenvalues and eigenvectors of the velocity gradient tensor $\nabla \boldsymbol{u}$ were calculated. They are tabulated in tables 3 and 4, respectively. The sum of the eigenvalues is zero, as required for an incompressible flow. Since the eigenvalues arise as a complex conjugate pair and a single real and

Re	$\lambda^c_{1,2}$	λ^c_3	$\lambda^{s_2}_{1,2}$	$\lambda^{s_2}_3$
215	-37.210 ± 21.35i	74.541	9.2565 ± 110.582i	-18.5131
220	-33.326 ± 62.38i	66.652	14.0702 ± 108.424i	-28.1404
240	-23.957 ± 138.17i	47.914	27.5823 ± 105.694i	-55.1646
275	-15.227 ± 202.15i	30.455	54.3772 ± 131.232i	-108.7545
300	-11.249 ± 228.13i	22.498	61.4271 ± 145.404i	-122.8542
400	-7.416 ± 293.83i	14.832	74.3162 ± 193.074i	-148.6324
500	-11.528 ± 367.86i	23.560	79.0853 ± 288.368i	-158.1706
700	-14.487 ± 544.69i	28.974	71.8950 ± 429.139i	-143.7900

TABLE 3. Eigenvalues of the velocity gradient tensor at the stagnation points c and s_2 in the cell centre and on the cell boundary, respectively.

Re	$\boldsymbol{v}^c_{1,2}$	$\boldsymbol{v}^c_3$
215	$(-0.5681 \pm 0.2739$i$, 0.2928 \pm 0.1600$i$, -0.7007)^{\mathrm{T}}$	$(0.9789, -0.0483, -0.1985)^{\mathrm{T}}$
220	$(-0.4217 \pm 0.4858$i$, 0.1786 \pm 0.3009$i$, -0.6809)^{\mathrm{T}}$	$(0.9407, -0.0501, -0.3355)^{\mathrm{T}}$
240	$(-0.4126 \pm 0.4686$i$, 0.1058 \pm 0.4035$i$, -0.6604)^{\mathrm{T}}$	$(0.8172, -0.0151, -0.5760)^{\mathrm{T}}$
275	$(-0.4643 \pm 0.3302$i$, 0.1157 \pm 0.4657$i$, -0.6671)^{\mathrm{T}}$	$(0.7399, 0.0175, -0.6724)^{\mathrm{T}}$
300	$(-0.4897 \pm 0.2484$i$, 0.1340 \pm 0.4808$i$, -0.6704)^{\mathrm{T}}$	$(0.7145, 0.0228, -0.6993)^{\mathrm{T}}$
400	$(-0.5458 \pm 0.0151$i$, 0.2049 \pm 0.4705$i$, -0.6623)^{\mathrm{T}}$	$(0.6538, -0.0122, -0.7566)^{\mathrm{T}}$
500	$(-0.5559 \pm 0.1004$i$, 0.2460 \pm 0.4516$i$, -0.6454)^{\mathrm{T}}$	$(0.6349, -0.0786, -0.7686)^{\mathrm{T}}$
700	$(-0.4995 \pm 0.1051$i$, 0.2300 \pm 0.4708$i$, -0.6818)^{\mathrm{T}}$	$(0.7319, -0.1682, -0.6603)^{\mathrm{T}}$
Re	$\boldsymbol{v}^{s_2}_{1,2}$	$\boldsymbol{v}^{s_2}_3$
215	$(-0.8809, 0.2671 \pm 0.3908i, 0.0000)^{\mathrm{T}}$	$(0.00, 0.000, 1.000)^{\mathrm{T}}$
220	$(-0.8582, 0.2588 \pm 0.4432i, 0.0000)^{\mathrm{T}}$	$(0.00, 0.000, 1.000)^{\mathrm{T}}$
240	$(-0.7668, 0.2603 \pm 0.5868i, 0.0000)^{\mathrm{T}}$	$(0.00, 0.000, 1.000)^{\mathrm{T}}$
275	$(-0.1191 \pm 0.5067$i$, 0.8538, 0.0000)^{\mathrm{T}}$	$(0.00, 0.000, 1.000)^{\mathrm{T}}$
300	$(-0.0639 \pm 0.4409$i$, 0.8953, 0.0000)^{\mathrm{T}}$	$(0.00, 0.000, 1.000)^{\mathrm{T}}$
400	$(-0.0151 \pm 0.2580$i$, 0.9660, 0.0000)^{\mathrm{T}}$	$(0.00, 0.000, 1.000)^{\mathrm{T}}$
500	$(-0.0395 \pm 0.2716$i$, 0.9616, 0.0000)^{\mathrm{T}}$	$(0.00, 0.000, 1.000)^{\mathrm{T}}$
700	$(-0.1066 \pm 0.4204$i$, 0.9011, 0.0000)^{\mathrm{T}}$	$(0.00, 0.000, 1.000)^{\mathrm{T}}$

TABLE 4. Normalized eigenvectors of the velocity gradient tensor at the stagnation points c and s_2 in the cell centre and on the cell boundary, respectively.

positive eigenvalue for all Reynolds numbers investigated, the central stagnation point is a saddle focus which spirals inward. From the normalized eigenvectors $\boldsymbol{v}^c_3$ it can be seen that the straining is approximately in x-direction for the smallest Reynolds number $Re = 215$. As the Reynolds number increases the straining direction approximately turns to the diagonal in the (x, z)-plane with $y \approx 0$.

The evolution of the character of the two kinds of fixed points in the two-dimensional subspace spanned by the two complex conjugate eigenvectors $\boldsymbol{e}_1$ and $\boldsymbol{e}_2$ is shown in figure 7 by displaying $\det(A) = \mathrm{Re}^2(\lambda) + \mathrm{Im}^2(\lambda)$ and $\mathrm{tr}(A) = 2\mathrm{Re}(\lambda)$ as functions of the Reynolds number, where A is the projection of the strain rate tensor onto the plane $(\boldsymbol{e}_1, \boldsymbol{e}_2)$. The inward-spiralling saddle focus in the cell centre evolves from the hyperbolic point of the basic state. The saddle focus comes into existence slightly above the threshold at $\epsilon = 0.0028$. The character of the saddle focus upon its creation and in linear approximation according to (4.1) is shown as a black dot in figure 7. It is consistent with the trend of the character obtained from the nonlinear

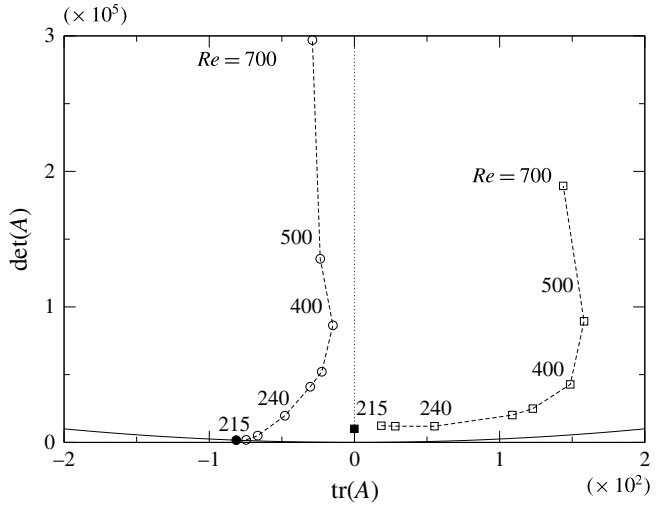

FIGURE 7. Determinant and trace of the velocity gradient tensor projected onto the subspace spanned by the two complex conjugate eigenvectors $(\boldsymbol{e}_1, \boldsymbol{e}_2)$ of the fixed points. The solid line indicates $\det(A) = \mathrm{tr}(A)^2/4$. Circles and squares relate to the saddle foci c and s_2, respectively. The Reynolds number are 215, 220, 240, 275, 300, 400, 500 and 700 (some are indicated by labels). The full square indicates the elliptic point of the neutrally stable basic state and the dot represents the slightly supercritical onset point of the central saddle focus approximated by (4.1).

solutions (circles): The reduction of the trace as Re increases indicates a tendency towards solid-body rotation in the cell centre. The outward-spiralling saddle focus on the cell boundary (squares in in figure 7) evolves from one of the elliptic points at criticality. It thus experiences the opposite trend: the strain in the subspace considered, and thus $\mathrm{tr}(A)$, increases rapidly with Reynolds number, but does not change much anymore beyond $Re \approx 400$.

4.3. *Relation between fixed points and limit cycles*

To further characterize the flow topology we focus on the representative case of $Re = 500$. In addition to the fixed points degenerate saddle limit cycles exist. We find two types of limit cycles on the walls. One type, denoted $w_{1,2}$, is made by the rectangles given by the intersection of each cell boundary with the walls. These wall limit cycles are saddle limit cycles which are attracting along the cell boundary (see figure 6) and repelling in the immediate vicinity of the walls.

The two unstable manifolds of w_1 and w_2 meets on the walls midway between both cell boundaries and represent the stable manifolds of another, non-trivial, degenerate saddle limit cycle w_c. To find it we consider the streamline pattern on the walls. The streamlines on the moving walls are straight and prescribed by the boundary conditions. Approximations to the streamlines on the stationary walls at $y = \pm 0.5$ were obtained by integrating the velocity field restricted to the planes $y = \pm 0.5 \mp 1.5 \times 10^{-4}$ and imposing $v = 0$. The distance from the wall corresponds to the locus of the first collocation point. The result is shown in figure 8(*a*). This approximation to the wall streamlines is in qualitative agreement with the deposition pattern of fine particles (figure 8*b*) which was observed experimentally by Blohm (2001) for $\Gamma = 1.96$. Streamlines on the moving walls with velocity $|\boldsymbol{u}| = Re$ are topologically connected

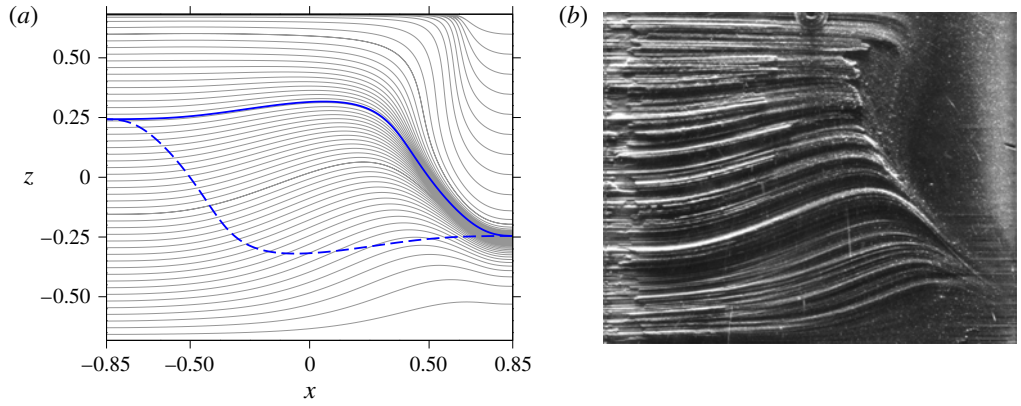

FIGURE 8. (Colour online) (*a*) Wall streamlines on the bottom of the cavity at $y=-1/2$ (grey) and projection of the closed streamline w_c on the wall (blue) for $Re=500$. Shown are the segments of the closed streamline on the bottom wall at $y=-0.5$ (full blue line) and on the top wall at $y=0.5$ (dashed blue line). (*b*) Photograph of the deposition pattern of tiny particles on the solid wall of an anti-symmetrically driven cavity with $\Gamma=1.96$ having been operated at $Re=700$ for a long period of time (from Blohm 2001). The visible lines can be interpreted as skin-friction lines.

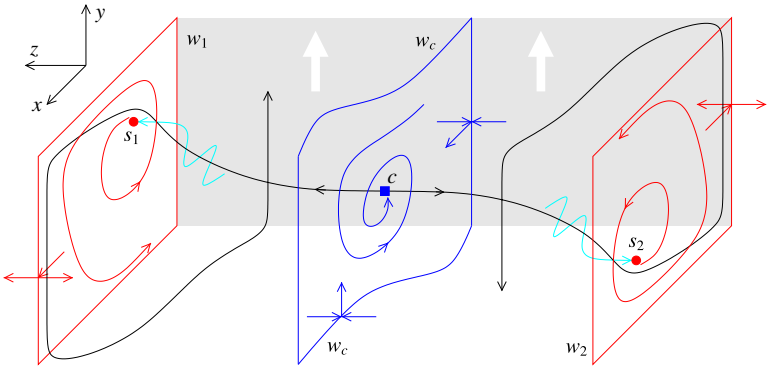

FIGURE 9. (Colour online) Sketch of the major topological elements for supercritical conditions with $Re \geqslant 215 > Re_c$. The central saddle focus (blue square) and the saddle limit cycle on the wall (blue) are denoted c and w_c, respectively, while the saddle foci on the cell boundaries (red dots) are indicated by s_1 and s_2 with corresponding saddle limit cycles $w_{1,2}$ (red). The grey rectangle in the background symbolizes the upward moving wall.

with the streamlines on the stationary walls with velocity $|\boldsymbol{u}|=0$. The motion on the four walls is thus degenerate in the sense that the velocity on the walls is stepwise constant with magnitude Re or zero.

To find w_c the fixed point of an iterative map was calculated using the start and end points of the computed streamlines on the stationary walls. The iterative map confirms the attraction of the saddle limit cycle w_c in the immediate vicinity of the wall and the repulsion into the fluid. The saddle limit cycle w_c is shown in blue in figure 8(*a*).

A sketch of all saddle foci and limit cycles is provided in figure 9. The direction of the two-dimensional unstable manifold of the central saddle limit cycle w_c (blue)

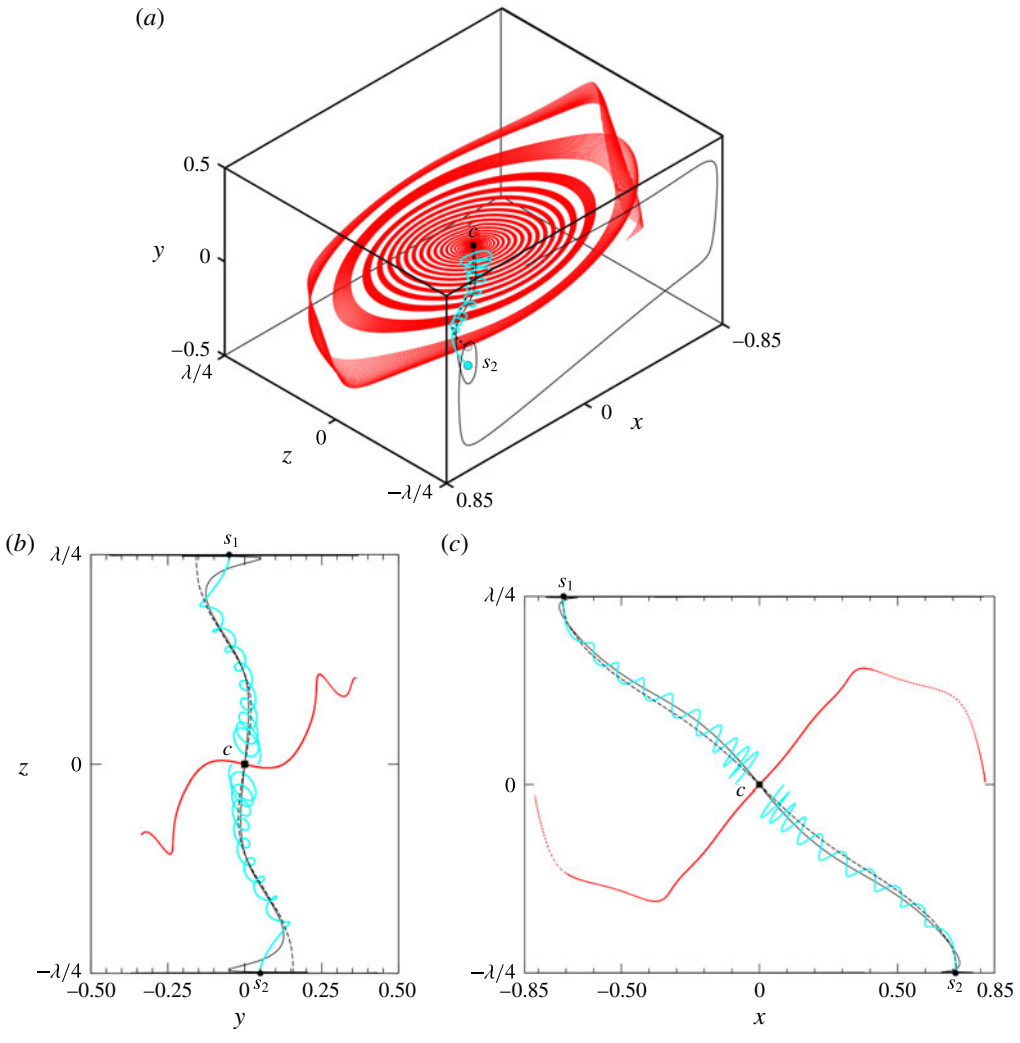

FIGURE 10. (*a*) Three-dimensional visualization of the stable (red) and unstable (solid black line) manifolds of the central saddle focus c (black dot) for $Re = 500$. The stable manifold of s_2 (cyan dot) is shown in cyan. The dotted line represents the vortex line through c; it ends orthogonally on the cell boundary (circle). (*b*,*c*) Show the intersection of the stable manifold of c with $x = 0$ (*b*) and $y = 0$ (*c*) as well as the projection to these planes of the lines shown in (*a*).

varies along the limit cycle, the arrows normal to w_c and normal to the wall in figure 9 are meant only symbolically.

For the advection organized by the saddle foci and saddle limit cycles it is useful to identify their stable and unstable manifolds and inquire about possible connections. The two-dimensional unstable manifolds of the saddle foci $s_{1,2}$ on the cell boundaries are made by the plane cell boundaries. They continue, via the rectangular wall limit cycles $w_{1,2}$, in $\pm z$-direction and meet at the central wall limit cycle w_c. Figure 10(*a*) shows a three-dimensional view of the stable two-dimensional manifold of the central saddle focus c (red) and one of its one-dimensional unstable manifolds (black line)

for $Re = 500$. In addition, the one-dimensional stable manifold of s_2 is shown in cyan. Clearly, the one-dimensional manifolds of c are distinct from those of s_1 and s_2 and thus are not directly connected with each other. In particular, the unstable manifolds of c do not end on the cell boundaries. This is consistent with the different evolution on a variation of Re of the two kinds of saddle foci originating from the elliptic and the hyperbolic points of the basic state at criticality. For a more quantitative representation figure 10(*b*,*c*) shows the intersections of the stable two-dimensional manifold of c (red line) with the planes $x = 0$ (figure 10*a*) and $y = 0$ (figure 10*b*). The projections of the two one-dimensional unstable manifolds of the saddle focus c are shown as black lines and those of s_1 and s_2 are displayed in cyan. In addition, the vortex line (dashed) which passes through c is shown in figure 10 to illustrate the alignment of the vorticity with the main strain direction in the nonlinear flow which is caused by the elliptic instability of the basic flow in which strain and vorticity are orthogonal. The intersections of the vortex line with the cell boundaries are distinct from the fixed points (also see table 2).

Since the one-dimensional manifolds of c, s_1 and s_2 are not connected their further evolution is of interest. To that end the two unstable manifolds of c and the stable manifold of s_2 have been computed forward and backward in time, respectively. The results are shown in figures 11(*a*) and 11(*b*), respectively. We find all one-dimensional manifolds (streamlines) to alternatingly spiral near the cell boundary and near the stable two-dimensional manifold of c. During their evolution all streamlines approach the central saddle limit cycle w_c (blue in figure 11) very closely or eventually terminate on the wall (before coming even closer to the wall limit cycle) signalling the resolution limit for the near-wall motion. To illustrate this the last part of the calculated streamline before termination is shown in cyan in figure 11(*b*).

4.4. *Heteroclinic tangling*

The close approach of all one-dimensional manifolds to the saddle limit cycle w_c signals its importance for the flow. This can be used to construct an approximation to the unstable two-dimensional manifold of w_c. To that end 1000 streamlines were computed forward and backward in time which are initialized equidistantly on a small circle about $\boldsymbol{x}_c = (0, 0, 0)$ with radius 2×10^{-4} in the plane $y = 0$. Figure 12 shows a Poincaré section of the streamlines on the plane $y = 0$. The Poincaré points of the streamlines backward in time (red) approximate the stable manifold of c. The streamlines forward in time are shown as small black dots. Initially, the streamlines separate into two streamline bundles, each approximating one of the two one-dimensional unstable manifolds of c. These streamline bundles extend towards the upper left and the lower right corners of the figure each producing indistinguishable Poincaré points, indicated by orange and magenta. The first Poincaré point is labelled '1'. In the course of their evolution the point clouds in the Poincaré plane resulting from the two streamline bundles become stretched. This effect becomes visible only when the bundles return close to the saddle focus for the first time (similar to figure 11*a*). For a better visibility of the early evolution the Poincaré points of one streamline out of each bundle is shown by orange and magenta dots, respectively, for the first 55 returns. After the second return to the cell boundaries the computed streamlines pass the central wall limit cycle w_c extremely closely and the streamline bundles become very much stretched. Due to the close approach to the wall limit cycle w_c the streamlines approximately lie on the unstable two-dimensional manifold of the wall limit cycle. From figure 12 this approximation of the unstable

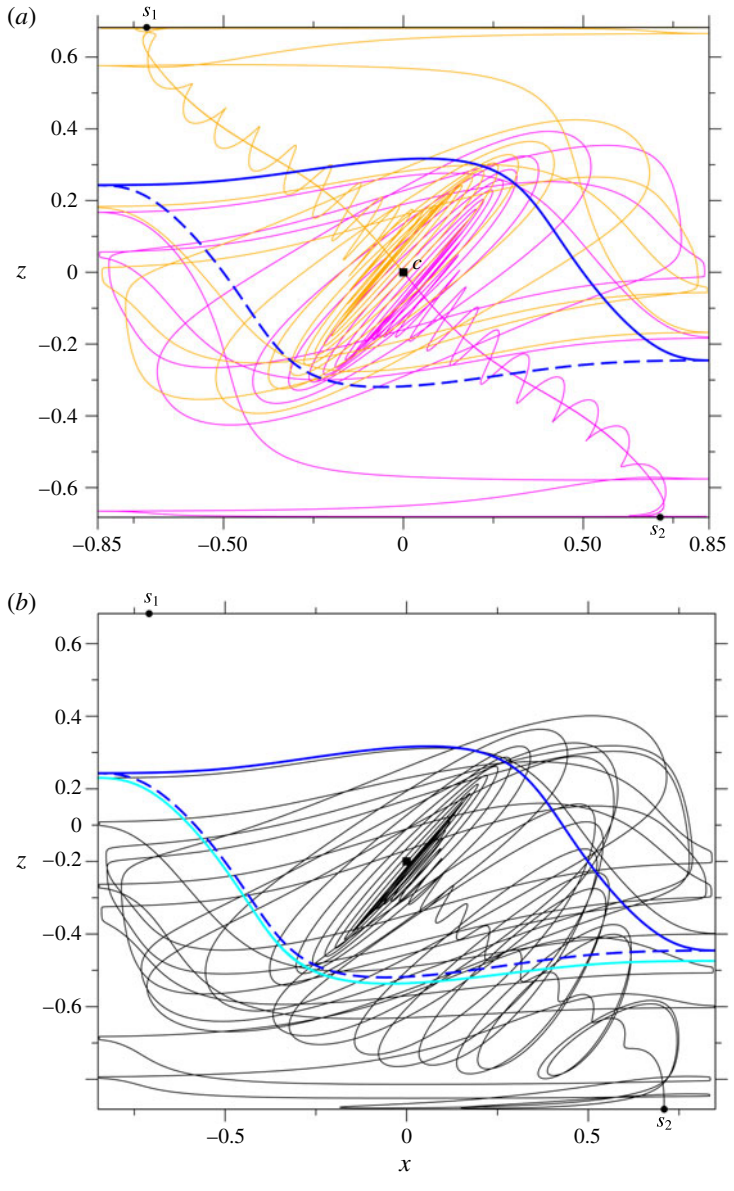

FIGURE 11. (*a*) Evolution of the two unstable manifolds of c (magenta and orange solid lines) for $Re = 500$. (*b*) Stable manifold of s_2 obtained by integration backward in time. The last part of the streamline, before ending (backward in time) on the boundary at $x = 0.85$, is shown in cyan. The blue full and dashed lines in (*a*,*b*) indicate the wall limit cycle w_c.

manifold of the wall limit cycle (black dots) intersects the stable manifold of the central saddle focus transversely in a tangled fashion. We thus conjecture the existence of a heteroclinic tangle between the two-dimensional stable manifold of c and the two-dimensional unstable manifold of w_c.

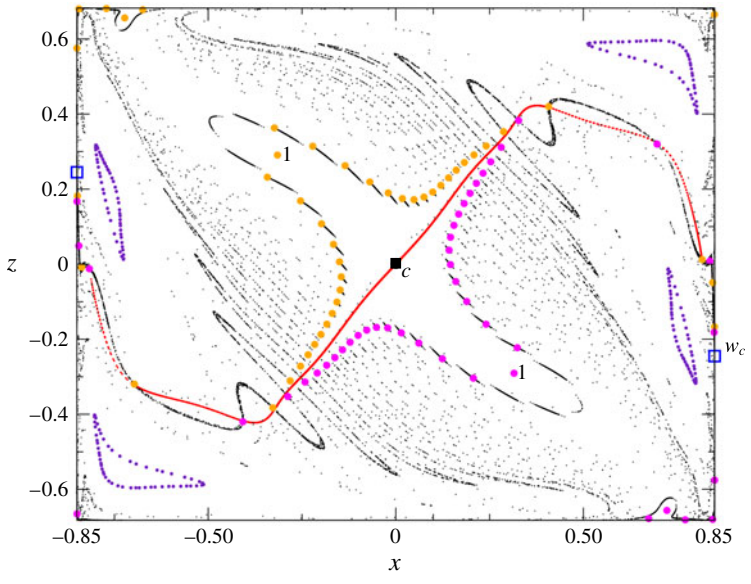

FIGURE 12. Transverse intersection in the Poincaré plane $y = 0$ of the two-dimensional stable manifold (red) of the central fixed point c and the unstable two-dimensional manifold (black dots) of the wall limit cycle w_c approximated by 1000 streamlines originating from the vicinity of the central saddle focus for $Re = 500$. The orange and magenta dots represent the 55 first returns to the Poincaré plane for two representative streamlines (out of 1000 initial conditions) which are initially moving close to the cell boundary at $z = 0.6825$ and $z = -0.6825$, respectively. The first return is labelled '1'. The blue squares indicate the location of the closed wall limit cycle w_c and the indigo dots delineate the largest reconstructible KAM tori which are discussed in § 4.5.

4.5. *KAM tori and chaotic sea*

The streamfunction of the basic two-dimensional flow can be interpreted as the Hamiltonian of a one-degree-of-freedom conservative dynamical system in which all fluid elements move on periodic orbits (Ottino 1989). For a three-dimensional steady flow the streamlines are typically quasi-periodic (regular) in a subvolume of the cell with chaotic streamlines coexisting in other parts of the domain. Based on the analogy between incompressible fluid flow and Hamiltonian systems (Bajer 1994) we denote the regions of regular motion as Kolmogorov–Arnold–Moser tori (KAM tori, Guckenheimer & Holmes 1983). They are embedded in the so-called sea of chaotic streamlines. If the Reynolds number is increased beyond it critical value the chaotic sea typically grows from the boundaries of the domain and continuously replaces the regular regions on a further increase of Re (Biemond *et al.* 2008).

The present system, however, behaves differently. Even for slightly supercritical conditions the whole volume is occupied by weakly chaotic streamlines. As the Reynolds number increases the chaos becomes stronger, but KAM tori appear and grow with Re until, for even higher Reynolds numbers, they start shrinking with Re. Due to their significance for mixing (Ottino & Khakhar 2000), particle accumulation (Mukin & Kuhlmann 2013; Muldoon & Kuhlmann 2013) and the transport in general we aim at identifying the most prominent KAM tori as a function of the Reynolds

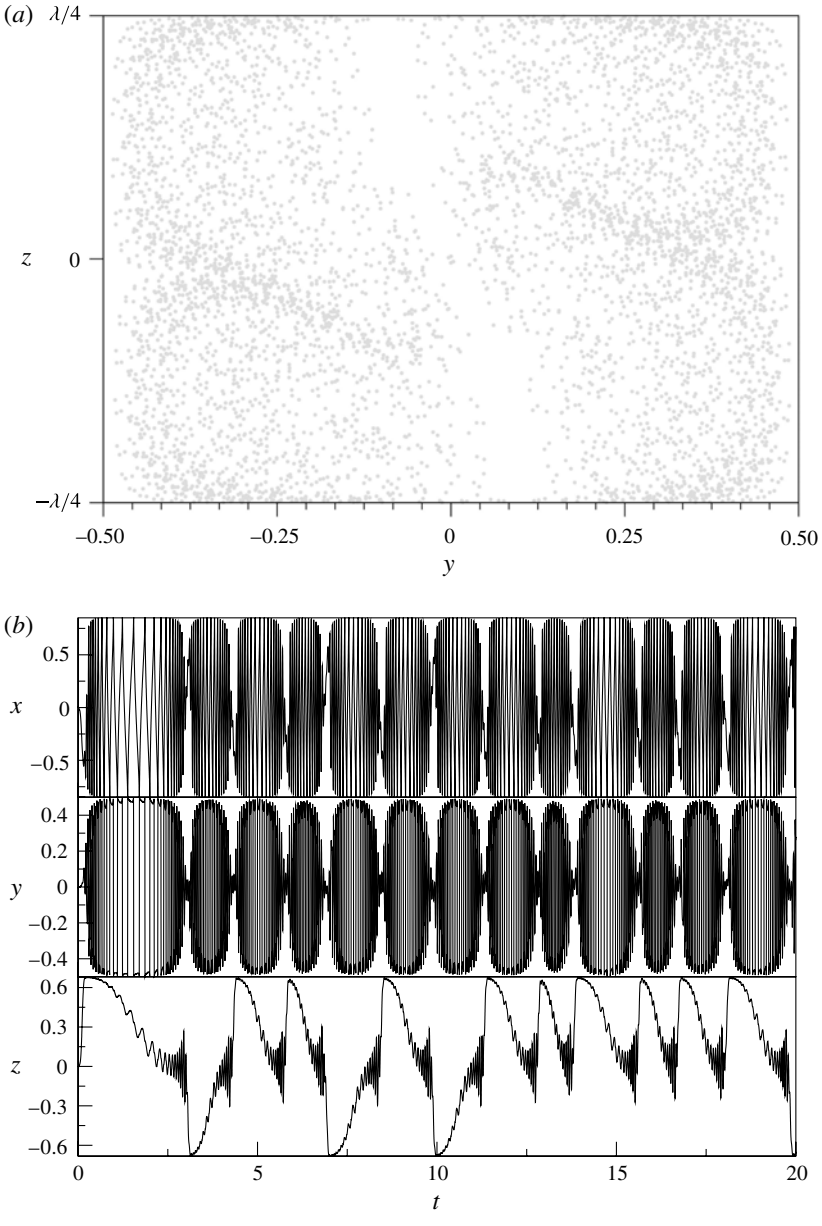

FIGURE 13. (*a*) Poincaré section on $x = 0$ for $Re = 240$ of two streamlines for $t = 100$ initialized at $(x, y, z) = (0, \pm 10^{-4}, \pm 10^{-3})$. (*b*) Coordinates of a fluid element initialized at $(x, y, z) = (0, 10^{-4}, 10^{-2})$ as functions of time.

number for $Re = 240$, 275, 300, 400, 500 and 700. Some technical detail are provided in § A.2.

Figure 13(*a*) shows a Poincaré section at $x = 0$ for $Re = 240$, which is only 13 % above the critical Reynolds number $Re_c = 211.53$. Obviously, all streamlines computed are chaotic, covering the whole cross-section. This behaviour is in marked

contradiction to what is expected from other systems like the Rayleigh–Bénard (Arter 1983) or the Taylor–Couette problem (Broomhead & Ryrie 1988) where most of the volume is occupied by regular streamlines slightly supercritically. The type of chaotic motion we find in the two-sided cavity is illustrated in figure 13(*b*) showing the evolution of a single streamline initiated at $t=0$ near $\boldsymbol{x}_c$ at $(x, y, z) = (0, 10^{-4}, 10^{-2})$. Whenever the fluid element moves near $\boldsymbol{x}_c$ it is rapidly transported to one of the cell boundaries from where it slowly returns to the centre, describing an overturning motion in the (x, y) plane. The nearly regular oscillations in the (x, y) plane are interrupted whenever the streamline returns to the middle of the cell ($z \approx 0$) upon which it spirals inward and approaches the central saddle focus c. Due to the high sensitivity of the motion near the fixed point c, it distributes the streamlines in a chaotic fashion resulting in a chaotic mixing within the whole periodic cell. The motion is only weakly chaotic in the sense that long periods of a relatively regular motion are interrupted by short excursions to the saddle focus c. The regular periods have different durations and arise either for $z>0$ or $z<0$ in an irregular fashion (see e.g. $t\approx 3$ and $t\approx 4.7$ in figure 13*b*).

A similar behaviour as for $Re = 240$ is also observed for $Re = 215$ (not shown). These results suggest that the flow becomes globally chaotic soon, if not immediately, beyond the onset of three-dimensional flow with a duration of the more or less regular bursts tending to infinity as the critical Reynolds number is approached from above. Apparently, the observed sensitivity of the streamlines is caused by the existence of the complex structure of saddle foci immediately above Re_c which emerge from the basic cat's-eye flow. The details of the streamline chaos near the threshold is complicated, however, by the structural changes of the fixed points in the flow which arise in a very narrow Reynolds number range near Re_c (see § 4.1).

As the Reynolds number is increased to $Re = 275$ two slender regular regions are born. They are demarcated by the two largest reconstructible KAM tori shown in figure 14. Within each convection cell we find two KAM tori which are point symmetric due to the symmetry of the flow. On a further increase of Re the KAM tori grow larger and, for $Re = 300$, regular islands arise due to a 5 : 1 resonance (figure 15). All KAM tori grow in size as the Reynolds number is increased further. For $Re=400$ the tori of each of the two point-symmetrically located sets have merged. The Poincaré section at $x=0$ and the KAM tori for $Re=400$ are shown in figure 16. The resulting KAM tori consist of a single pair only of point-symmetrically placed simply periodic tori.

For $Re=500$ a similar streamline topology is found (figure 17, see also figure 12 for a Poincaré section at $y=0$). However, the regular regions have shrunk in size. This trend continues up to the largest Reynolds number considered, $Re=700$. The KAM tori for this Reynolds number are very slender with the chaotic sea occupying most of the domain (figure 18). Each set of tori consists of a major simply periodic torus (purple) and another doubly periodic torus (green) which is wound once about the major torus. The winding is particularly strong (visible) near the walls at $x=\pm 0.85$ where the vorticity is highest. The absence of secondary winding tori for $Re=500$ indicates that a splitting of the purple KAM tori (2 : 1 resonance) must have taken place at an intermediate Reynolds number.

As pointed out by Mukin & Kuhlmann (2013) and Muldoon & Kuhlmann (2013) an important property of the regular structures of steady three-dimensional flows in closed domains is the minimum distance Δ_ψ of the closed streamlines from the boundaries. Depending on Δ_ψ, finite size particles may be attracted to the regular regions by way of particle–boundary interactions (Hofmann & Kuhlmann 2011). Moreover, Kuhlmann

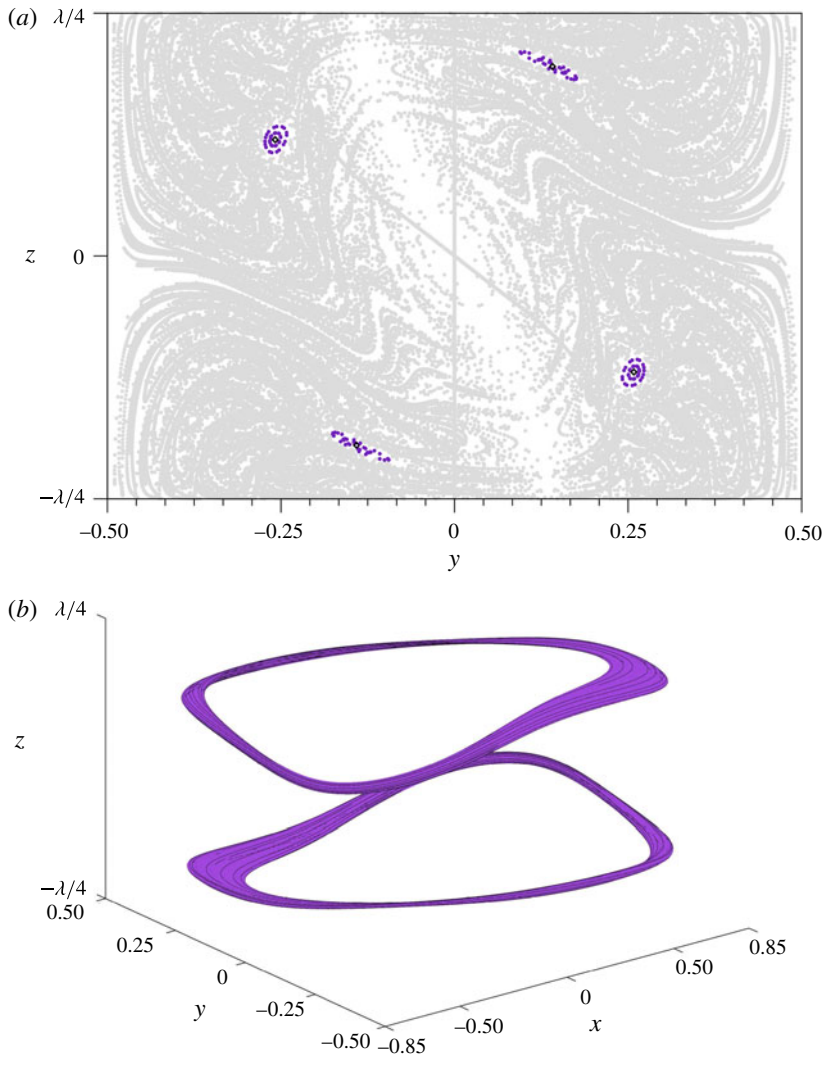

FIGURE 14. (Colour online) (*a*) Poincaré section on $x = 0$ for $Re = 275$. Grey points indicate chaotic streamlines. The closed streamlines in the centre of the KAM tori (purple dots) are marked by black diamonds (◇). (*b*) Three-dimensional representation of the largest reconstructible KAM tori. The axes are not to scale.

et al. (2016) have provided strong evidence that Δ_ψ can be used to guide particles selection in order to observe particle accumulation structures experimentally. With this perspective in mind the location of the KAM tori with respect to the boundaries is an important property of the flow. We find the KAM tori for $Re \geqslant 300$ to always remain more or less localized near the cavity walls and the periodic cell boundaries. Within each set of nested KAM tori we find a single closed streamline. It is indicated by diamonds (◇) in the above Poincaré cuts. The closed streamlines are located by first approximately identifying elliptical fixed points of the Poincaré map. Thereafter, the coordinates of the fixed points in the Poincaré plane are computed with an accuracy of 10^{-4} using Newton–Raphson iteration.

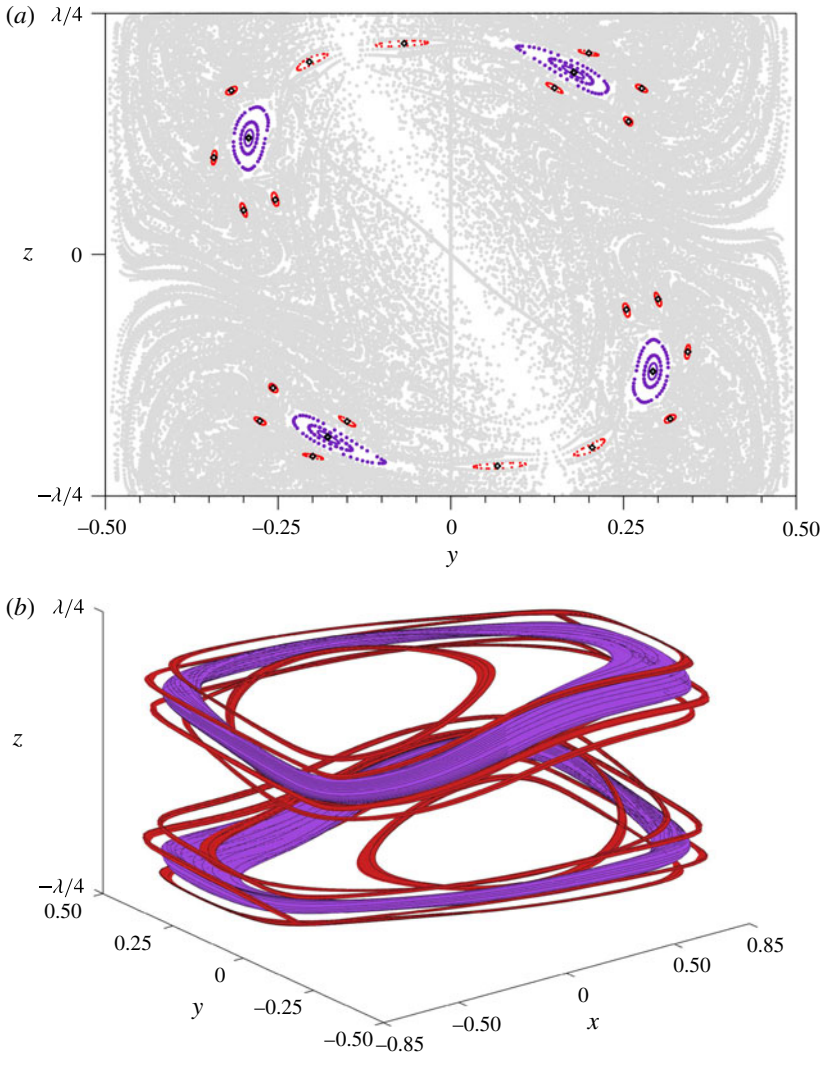

FIGURE 15. (Colour online) (*a*) Poincaré section on $x = 0$ for $Re = 300$. Grey points indicate chaotic streamlines. The closed streamlines at the centre of the KAM tori (purple dots) are marked by black diamonds (◇). (*b*) Three-dimensional representation of the largest reconstructible KAM tori. The axes are not to scale.

Figure 19(*a*,*b*) shows projections onto the (y, z)-plane of the closed streamlines inside of the KAM tori. The projections onto the (x, z)-plane are shown in figure 19(*c*,*d*), and three-dimensional views are depicted in figure 19(*e*,*f*). The minimum distance of any closed streamline from the boundary always occurs near the moving walls at $x = \pm 0.85$. The numerical data for the minimum distance Δ_ψ are provided in table 5 together with the respective orbit times τ. For the closed streamlines L_i^j and the largest KAM torus T_i^j identified we indicate with j the winding number around the main KAM torus and with i the turnover period. Since the regular structures arise as a point-symmetric pair, the fixed points on $x = 0$ for the closed streamlines are provided only for $z > 0$.

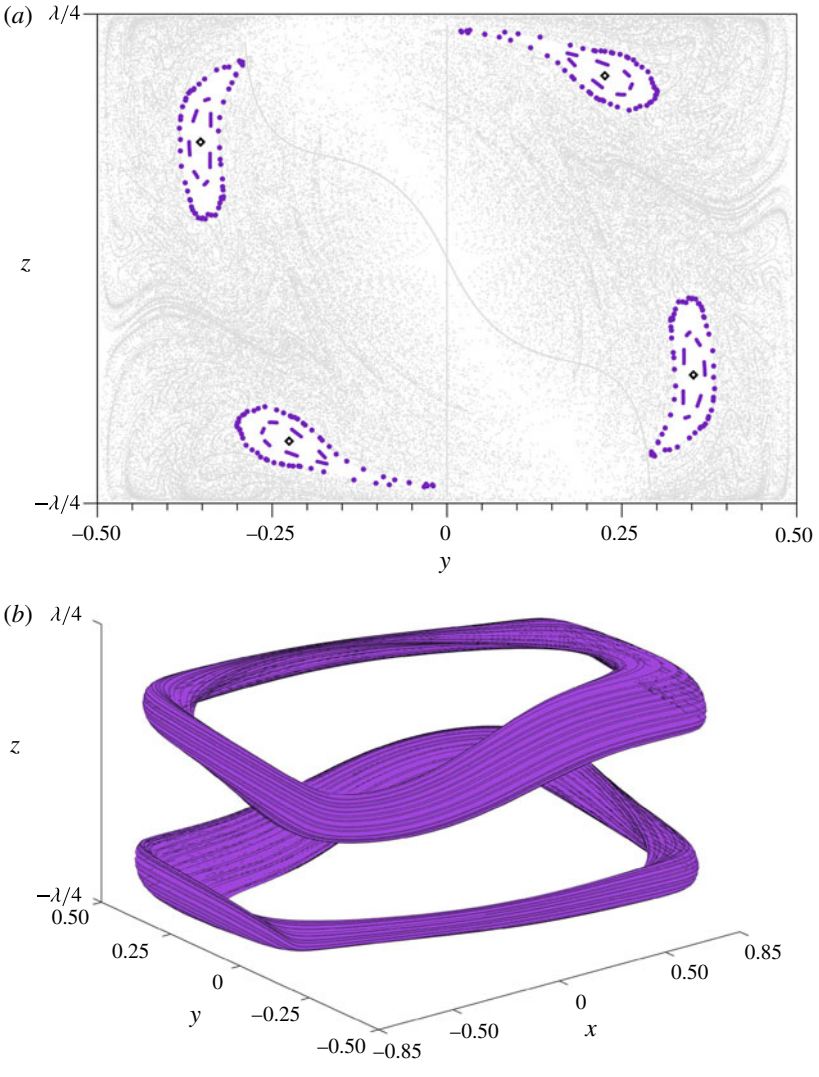

FIGURE 16. (Colour online) (*a*) Poincaré section on $x = 0$ for $Re = 400$. Grey points indicate chaotic streamlines. The closed streamlines at the centre of the KAM tori (purple dots) are marked by black diamonds (◇). (*b*) Three-dimensional representation of the largest reconstructible KAM tori. The axes are not to scale.

5. Discussion and conclusions

The streamline topology of the steady three-dimensional cellular flow in a two-sided anti-parallel lid-driven cavity has been investigated for aspect ratio $\Gamma = 1.7$. Steady flows for several Reynolds numbers above the critical onset of three-dimensional flow were obtained from numerical long-time solutions of the Navier–Stokes equations using the spectral method of Albensoeder & Kuhlmann (2005).

For all Reynolds numbers for which numerical simulations were carried out, $Re =$ 215, 220, 240, 275, 300, 400, 500 and 700, the supercritical three-dimensional cellular flow exhibits a point symmetry with respect to the periodic free stagnation points in the centres of each convection cell and a mirror symmetry with respect to the flat

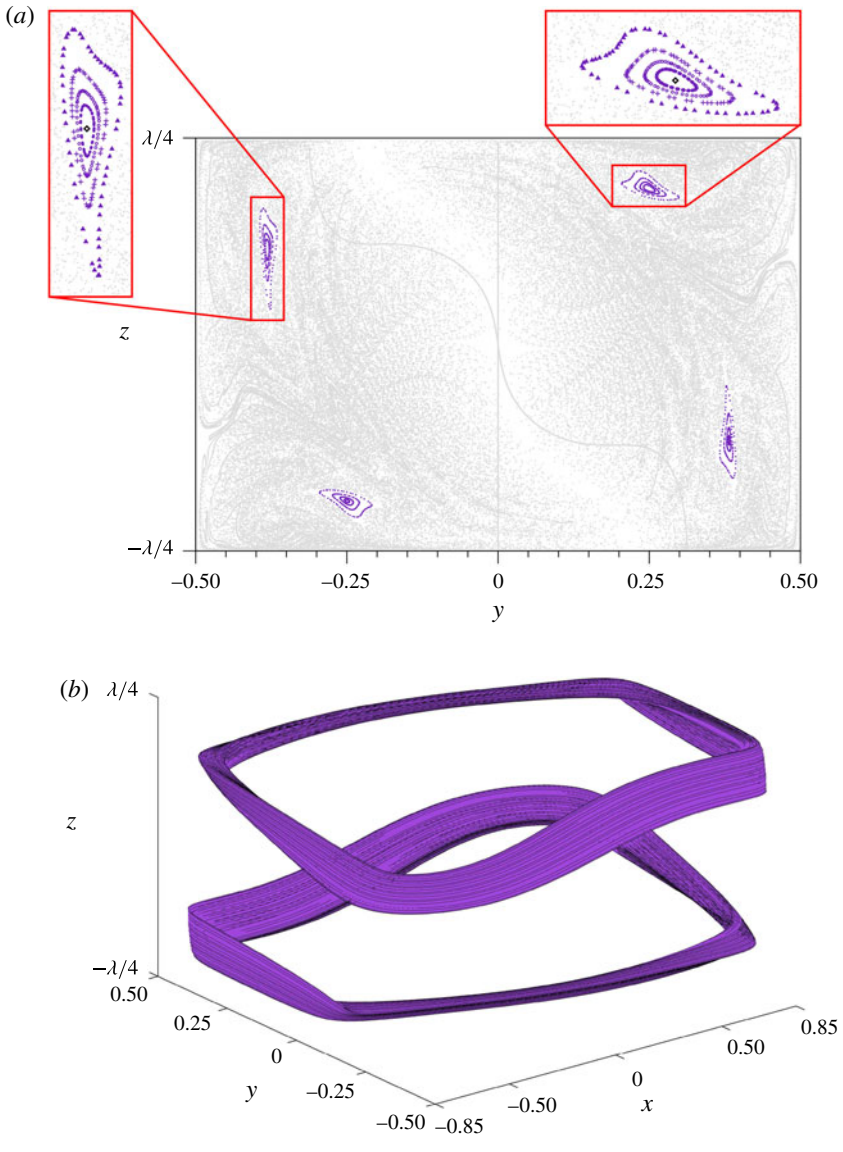

FIGURE 17. (Colour online) (*a*) Poincaré section on $x = 0$ for $Re = 500$. Grey points indicate chaotic streamlines. The closed streamlines at the centre of the KAM tori (purple dots) are marked by black diamonds (◇). (*b*) Three-dimensional representation of the largest reconstructible KAM tori. The axes are not to scale.

cell boundaries at $z = \pm(1 + 2n)\lambda/4$ with $n \in \mathbb{N}$. At the onset of three-dimensional flow the three periodic lines due to the two elliptic and the hyperbolic points of the basic flow change into two hyperbolic points, one in the cell centre and one on each cell boundary, and two saddle foci on each cell boundary. These fixed points undergo a very rapid transformation within $Re \in [Re_c, 1.0127 \times Re_c]$ such that the central hyperbolic point becomes a spiralling-in saddle focus and while the hyperbolic points on the cell boundaries merge with one of the saddle foci an thus annihilating

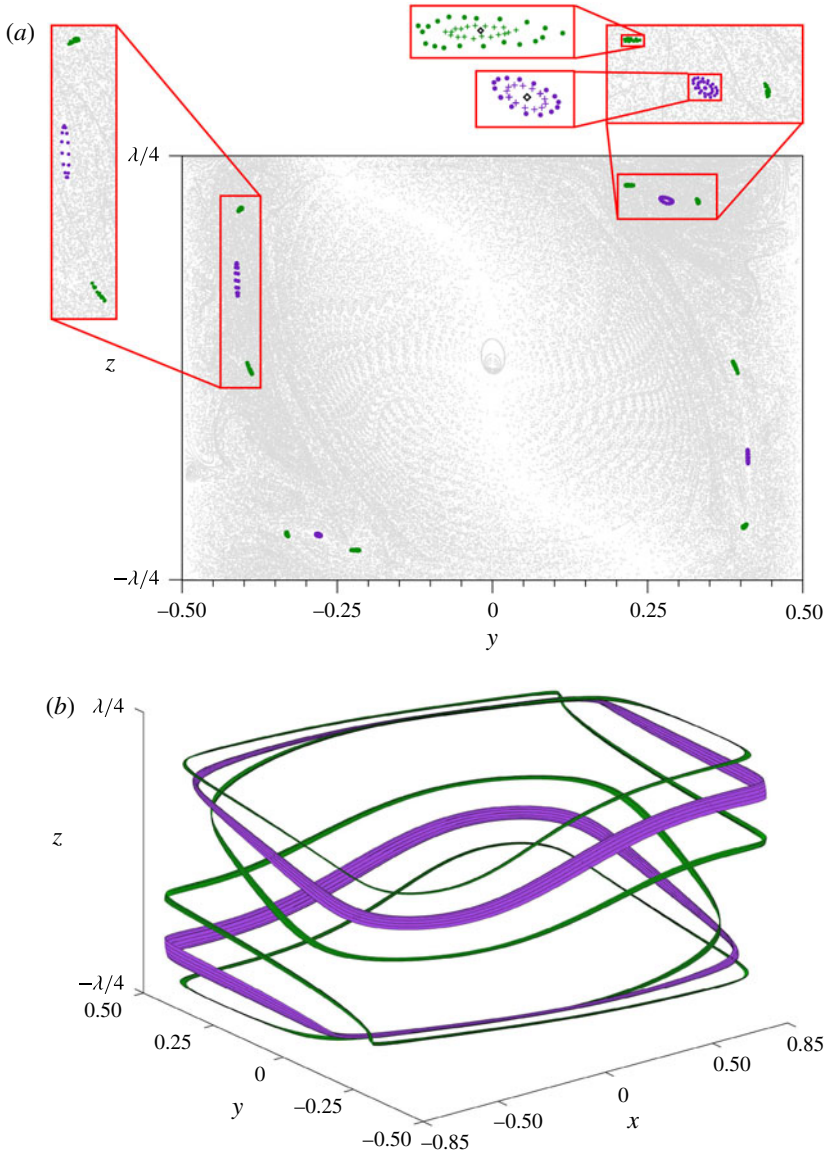

FIGURE 18. (Colour online) (*a*) Poincaré section on $x = 0$ for $Re = 700$. Grey points indicate chaotic streamlines. The closed streamlines at the centre of the KAM tori (purple and green dots) are marked by black diamonds (◇). (*b*) Three-dimensional representation of the largest reconstructible KAM tori. The axes are not to scale.

each other. Apart from the degenerate rectangular saddle limit cycles made by the edges of the cell boundaries a non-trivial degenerate saddle limit cycle exists on the solid walls in the middle of each cell for all supercritical Reynolds numbers. The set of fixed points and limit cycles for $Re > 1.0127 \times Re_c$ exist in the steady flow for a wide range of supercritical Reynolds numbers. For the representative Reynolds number

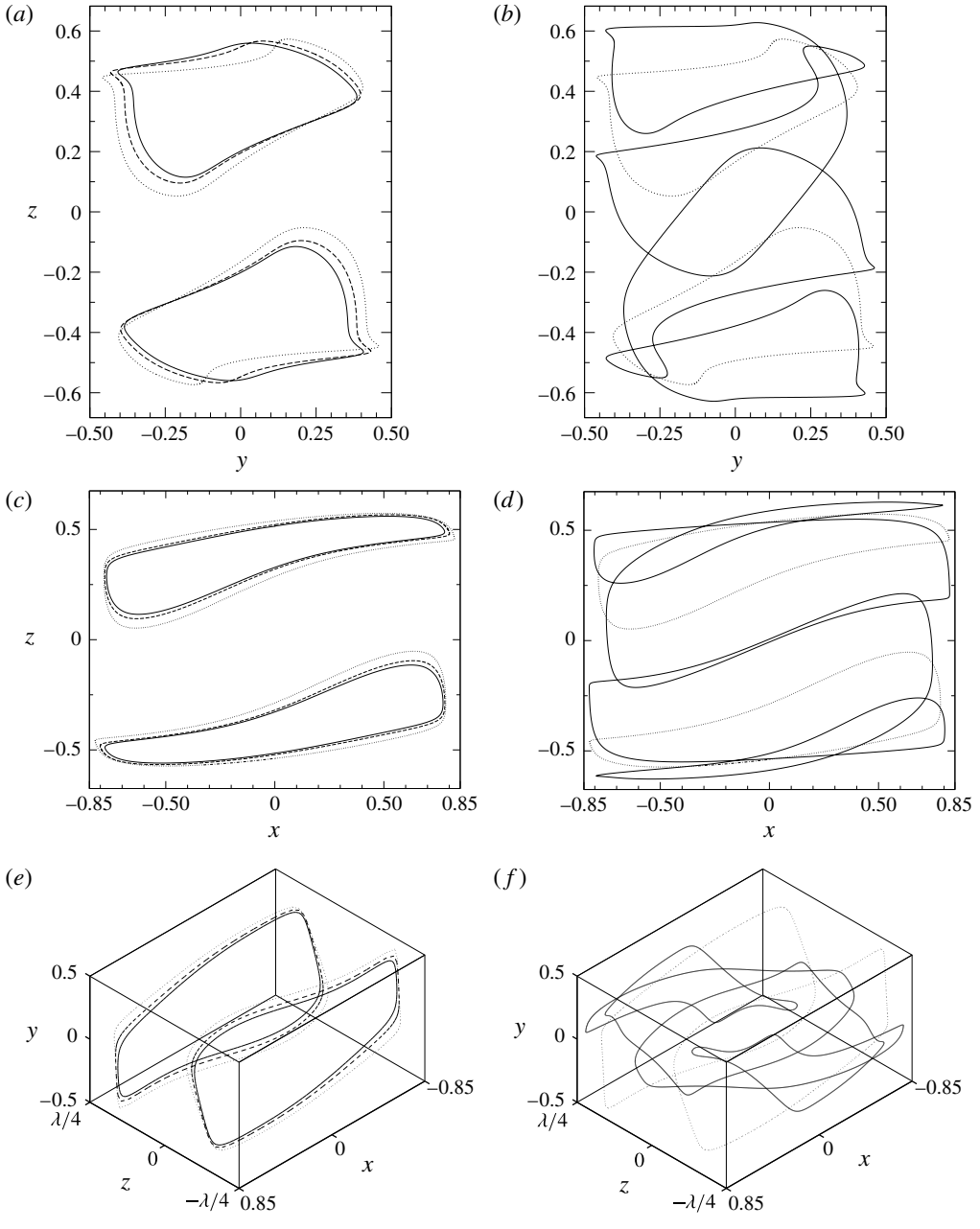

FIGURE 19. Closed streamlines for $Re = 400$, 500 and 700 (without the winding streamlines) (a,c,e) and for $Re = 700$ (b,d,f) including the closed winding streamlines. Projection on the (y, z)-plane: (a,b), projection on the (x, z)-plane: (c,d) and three-dimensional visualization: (e,f). The solid line denotes $Re = 400$, the dashed line $Re = 500$ and the dotted line $Re = 700$ in (a,c,e). In (b,d,f) we denote the single-periodic orbits with dotted lines and the double-periodic orbits with solid lines for $Re = 700$.

Re	KAM/streamline	τ	Δ_T	Δ_ψ	Fixed point on $x=0$
275	T_1^0/L_1^0	0.0558	0.0920	0.1239	(0, 0.1424, 0.5329)
300	T_1^0/L_1^0	0.0478	0.0738	0.1019	(0, 0.1781, 0.5160)
	T_5^1/L_5^1	0.2275	0.0463	0.0498	(0, 0.2001, 0.5701)
400	T_1^0/L_1^0	0.0342	0.0349	0.0711	(0, 0.2257, 0.5153)
500	T_1^0/L_1^0	0.0272	0.0359	0.0493	(0, 0.2497, 0.5348)
700	T_1^0/L_1^0	0.0198	0.0243	0.0264	(0, 0.2809, 0.5345)
	T_2^1/L_2^1	0.0457	0.0233	0.0244	(0, 0.2210, 0.5838)

TABLE 5. Minimum distances Δ_T and Δ_ψ from the moving walls of the outermost KAM surface T_i^j and the corresponding closed streamline L_i^j, respectively, for different Reynolds numbers. In addition, the orbit time τ of the closed streamline is provided as well as one of the fixed points in the $(x=0)$-Poincaré plane corresponding to L_i^j.

of $Re = 500$ the unstable manifold of the non-trivial saddle limit cycle on the walls makes a heteroclinic tangle with the stable manifold of the central saddle focus and is thus identified as a cause of the streamline chaos.

If the tangling would have originated from a heteroclinic connection at a lower Reynolds number the flow within each cell would have been completely separated into two subvolumes without any exchange. This is not observed, however, at slightly supercritical Reynolds numbers. Rather, the streamlines occupy the whole cell moving close to both of the cell boundaries (cf. figure 13*b*). It is thus anticipated that a heteroclinic connection of the two manifolds does not exist at any Reynolds number. This behaviour is in marked contrast to what is typically observed in incompressible flows: within the generic scenario chaotic streamlines invade the flow domain from heteroclinic connections. Examples for such heteroclinic connections are separating streamlines in two-dimensional flow (Biemond *et al.* 2008), the cell boundaries of convection cells in Rayleigh–Bénard convection (Arter 1983), the boundaries of Taylor vortices (Broomhead & Ryrie 1988), the separatrix in the axisymmetric flow inside a spherical translating droplet (Kroujiline & Stone 1999) and the separatrix in axisymmetric vortex-breakdown bubbles (Sotiropoulos *et al.* 2001). Upon three-dimensional perturbations of all these flows the streamline chaos gradually grows from the heteroclinic connection. The present two-sided lid-driven cavity at $\Gamma = 1.7$ behaves differently: chaos does not gradually invade the regular region. It rather arises globally and space filling even for weakly three-dimensional flow, because no heteroclinic connection exists. Thus the two-sided lid-driven cavity represents another class of systems in which streamline chaos sets in globally.

Interestingly, regular regions are born upon an increase of Re, despite of the global streamline chaos at onset. We conjecture the reduction of the number of singular points by the merger of the hyperbolic point h and the saddle focus s' on the cell boundaries causes the regularization of the flow for increasing Reynolds numbers in the range $Re \in [240, 400]$. The regular regions created undergo the typical resonances before they shrink for relatively high Reynolds number to eventually disappear completely. The structure and location of the regular regions has been considered in detail, because they are of key importance not only for mixing, but also for the motion and accumulation of nearly density-matched particles of finite size (Schwabe *et al.* 2007). Hofmann & Kuhlmann (2011) have shown that the perturbation of the motion

of finite-size particles induced by domain boundaries can lead to a demixing of particles which then accumulate in or near the regular regions of the flow. This effect has been demonstrated to be the primary reason for demixing in thermocapillary liquid bridges by Mukin & Kuhlmann (2013) and Muldoon & Kuhlmann (2016). Evidence for the same mechanism of particle segregation in lid-driven cavities has been provided by Kuhlmann *et al.* (2016). It would thus be interesting to study in more detail the finite-size particle motion in the present system, based on the streamline topology uncovered.

Acknowledgement

The authors are very grateful for helpful and inspiring discussions with C. Kühn.

Appendix A

A.1. *Integration of streamlines*

The integration of streamlines requires a flow field interpolation. Keeping the relative and absolute tolerances in the Dormand–Prince method constant at 10^{-10}, three interpolation methods are tested. The first (reference) method consists of a fully spectral Chebyshev–Gauss–Lobatto interpolation in x- and y-directions and a Fourier interpolation in z using all $128 \times 128 \times 128$ modes. In the second method the data on the spectral collocation nodes are interpolated linearly and as a third case we consider a linear interpolation on an evenly spaced mesh of $150 \times 150 \times 150$ grid points, where the data on the grid points are obtained from the above spectral interpolation.

While using the spectral interpolation for all 2500 streamlines per Poincaré section is computationally too expensive, it can reasonably be applied to a few streamlines in a region of regular flow. Figure 20 shows the resulting Poincaré points. The black dots were obtained using the fully spectral interpolation. They delineate a KAM torus for $Re = 700$. The last two returns to the Poincaré plane are shown as open circles to indicate the magnitude of the numerical error. In addition, Poincaré points obtained using a linear interpolation on the spectral grid and using a linear interpolation on an equidistant 150^3 grid are shown as open squares in (*a*) and open diamonds in (*b*), respectively. The scatter of the data shows that the numerical error due to the linear interpolation on a spectral grid using $128^3 = 2\,097\,152$ grid points (*a*) is slightly larger than the one due to the fully spectral interpolation. However, the error for the linear interpolation on the equidistant grid (*b*) is much larger, even though more ($150^3 = 3\,375\,000$) grid points have been used. Thus the linear interpolation on an equidistant grid is not suitable for the integration of streamlines on the required time scales.

The above tests demonstrate the general accuracy requirements for computing streamlines in three-dimensional incompressible steady flows with a KAM structure. Based on these results the linear interpolation on the spectral grid is only employed for integrating chaotic streamlines when Poincaré sections are produced to identify the chaotic sea. For computing regular streamlines and producing the tabulated quantitative data, however, always the fully spectral interpolation is used.

A.2. *Poincaré plots and KAM surfaces*

For $Re = 275$, 300, 400 and 500, there are 2500 streamlines initialized and equidistantly distributed along the line $(x, y) = (0, 0)$ and $z \in [-\lambda/4, \lambda/4]$. As explained in § 4.5, less initial conditions are used for $Re = 240$. For $Re = 700$, 2500

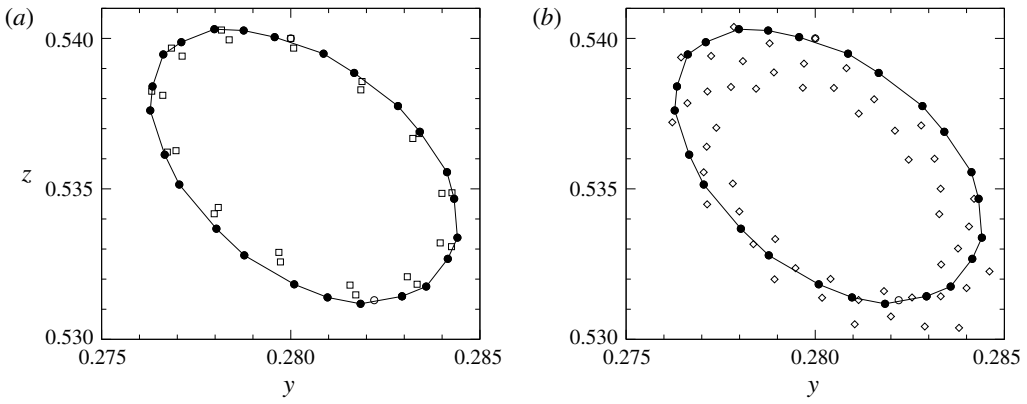

FIGURE 20. Poincaré sections at $x = 0$ for $Re = 700$ using different interpolation schemes. Poincaré points obtained from the 128^3 spectral interpolation of the flow field are shown by black dots in both (*a*,*b*). The closed polygon serves as a guide to the eye, where the two last Poincaré points (open circles) have been excluded to indicate the magnitude of the error. Open squares in (*a*) result from a linear interpolation on the spectral grid. Poincaré points resulting from a linear flow field interpolation on 150^3 equidistant grid points (open diamonds) are displayed in (*b*).

initial conditions are selected equidistantly on $(y, z) = (0, 0)$ within the segment $x \in [-0.85, 0]$.

From all streamlines, computed up to $t = 1$, Poincaré sections are constructed in the plane $x = 0$ disregarding the direction in which the Poincaré plane is crossed. Depending on the distribution of the Poincaré points they are assigned either to a KAM torus or to the chaotic sea. Additional streamlines are computed in the regular regions up to $t = 2$ for $Re = 400$ and 500 and $t = 3$ for $Re = 275$, 300 and 700 in order to aid the visualization of the contours of the KAM tori in the Poincaré plane. From the regular streamlines three-dimensional tori are constructed. To that end the central closed streamline of each KAM torus is calculated. Then hundred points evenly distributed along the closed streamline are defined together with the planes normal to the closed streamline in these points. Integrating a streamline belonging to the largest identifiable KAM torus for a time longer than the turnover time, multiple intersections with each of the hundred planes normal to the closed streamline are obtained. The cross section of the KAM tube is then reconstructed by interpolating all intersection points in a cross-sectional plane using cubic splines. Multivariate cubic Hermite splines are then employed to reconstruct each KAM surface from the corresponding cross-sectional interpolations.

REFERENCES

AIDUN, C. K., TRIANTAFILLOPOULOS, N. G. & BENSON, J. D. 1991 Global stability of a lid-driven cavity with throughflow: flow visualization studies. *Phys. Fluids* **3** (9), 2081–2091.

ALBENSOEDER, S. & KUHLMANN, H. C. 2002 Linear stability of rectangular cavity flows driven by anti-parallel motion of two facing walls. *J. Fluid Mech.* **458**, 153–180.

ALBENSOEDER, S. & KUHLMANN, H. C. 2003 Stability balloon for the double-lid-driven cavity flow. *Phys. Fluids* **15**, 2453–2456.

ALBENSOEDER, S. & KUHLMANN, H. C. 2005 Accurate three-dimensional lid-driven cavity flow. *J. Comput. Phys.* **206** (2), 536–558.

ALBENSOEDER, S. & KUHLMANN, H. C. 2006 Nonlinear three-dimensional flow in the lid-driven square cavity. *J. Fluid Mech.* **569**, 465–480.

ALBENSOEDER, S., KUHLMANN, H. C. & RATH, H. J. 2001*a* Multiplicity of steady two-dimensional flows in two-sided lid-driven cavities. *Theor. Comput. Fluid Dyn.* **14**, 223–241.

ALBENSOEDER, S., KUHLMANN, H. C. & RATH, H. J. 2001*b* Three-dimensional centrifugal-flow instabilities in the lid-driven-cavity problem. *Phys. Fluids* **13** (1), 121–135.

ALLEBORN, N., RASZILLIER, H. & DURST, F. 1999 Lid-driven cavity with heat and mass transport. *Intl J. Heat Mass Transfer* **42** (5), 833–853.

ANDERSON, P. D., GALAKTIONOV, O. S., PETERS, G. W. M., VAN DE VOSSE, F. N. & MEIJER, H. E. H. 2000 Chaotic fluid mixing in non-quasi-static time-periodic cavity flows. *Intl J. Heat Fluid Flow* **21** (2), 176–185.

AREF, H. 1984 Stirring by chaotic advection. *J. Fluid Mech.* **143**, 1–21.

AREF, H. 1990 Chaotic advection of fluid particles. *Phil. Trans. R. Soc. Lond.* A **333** (1631), 273–288.

ARTER, W. 1983 Ergodic stream-lines in steady convection. *Phys. Lett.* A **97**, 171–174.

BAJER, K. 1994 Hamiltonian formulation of the equations of streamlines in three-dimensional steady flows. *Chaos Solitons Fractals* **4** (6), 895–911.

BATCHELOR, G. K. 1956 On steady laminar flow with closed streamlines at large Reynolds number. *J. Fluid Mech.* **1**, 177–190.

BAYLY, B. J. 1986 Three-dimensional instability of elliptical flow. *Phys. Rev. Lett.* **57**, 2160–2163.

BENJAMIN, D. F., ANDERSON, T. J. & SCRIVEN, L. E. 1995 Multiple roll systems: steady-state operation. *Am. Inst. Chem. Engrs J.* **41** (5), 1045–1060.

BERRUT, J.-P. & TREFETHEN, L. N. 2004 Barycentric Lagrange interpolation. *SIAM Rev.* **46** (3), 501–517.

BIEMOND, J. J. B., DE MOURA, A. P. S., KÁROLYI, G., GREBOGI, C. & NIJMEIJER, H. 2008 Onset of chaotic advection in open flows. *Phys. Rev.* E **78**, 016317.

BLOHM, C. 2001 Experimentelle Untersuchung stationärer und zeitabhängiger Strömungen im zweiseitig angetriebenen Rechteckbehälter. PhD thesis, University of Bremen.

BLOHM, C. H. & KUHLMANN, H. C. 2002 The two-sided lid-driven cavity: experiments on stationary and time-dependent flows. *J. Fluid Mech.* **450**, 67–95.

BOTELLA, O. 1998 Résolution numérique de problèmes de Navier–Stokes singuliers par une méthode de projection tchebychev. PhD thesis, Université de Nice.

BOTELLA, O. & PEYRET, R. 1998 Benchmark spectral results on the lid-driven cavity flow. *Comput. Fluids* **27** (4), 421–433.

BOTELLA, O. & PEYRET, R. 2001 Computing singular solutions of the Navier–Stokes equations with the Chebyshev-collocation method. *Intl J. Numer. Meth. Fluids* **36** (2), 125–163.

BOYLAND, P. L., AREF, H. & STREMLER, M. A. 2000 Topological fluid mechanics of stirring. *J. Fluid Mech.* **403**, 277–304.

BRØNS, M. & HARTNACK, J. N. 1999 Streamline topologies near simple degenerate critical points in two-dimensional flow away from boundaries. *Phys. Fluids* **11**, 314–324.

BROOMHEAD, D. S. & RYRIE, S. C. 1988 Particle paths in wavy vortices. *Nonlinearity* **1** (3), 409–434.

BRUNEAU, C.-H. & SAAD, M. 2006 The 2d lid-driven cavity problem revisited. *Comput. Fluids* **35** (3), 326–348.

BURGGRAF, O. R. 1966 Analytical and numerical studies of the structure of steady separated flows. *J. Fluid Mech.* **24**, 113–151.

CANUTO, C., HUSSAINI, M. Y., QUARTERONI, A. & ZANG, T. A. 1988 *Spectral Methods in Fluid Dynamics*. Springer.

CHERNIKOV, A. A. & SCHMIDT, G. 1992 Chaotic streamlines in convective cells. *Phys. Lett.* A **169**, 51–56.

CHIEN, W.-L., RISING, H. & OTTINO, J. M. 1986 Laminar mixing and chaotic mixing in several cavitiy flows. *J. Fluid Mech.* **170**, 355–377.

CONTRERAS, P. S., DE LA CRUZ, L. M. & RAMOS, E. 2016 Topological analysis of a mixing flow generated by natural convection. *Phys. Fluids* **28** (1), 013602.

CRIGHTON, D. G. 1991 Airframe noise. In *Aeroacoustics of Flight Vehicles: Theory and Practice. Volume 1: Noise Sources* (ed. H. H. Hubbard), vol. 1, pp. 391–447. NASA Office of Management, Scientific and Technical Information Program.

DOMBRE, T., FRISCH, U., GREENE, J. M., HÉNON, M., MEHR, A. & SOWARD, A. M. 1986 Chaotic streamlines in the ABC flows. *J. Fluid Mech.* **167**, 353–391.

DOMINGUEZ-LERMA, M. A., CANNELL, D. S. & AHLERS, G. 1986 Eckhaus boundary and wavenumber selection in rotating Couette–Taylor flow. *Phys. Rev.* A **34**, 4956–4970.

DORMAND, J. R. & PRINCE, P. J. 1980 A family of embedded Runge–Kutta formulae. *J. Comput. Appl. Maths* **6** (1), 19–26.

FREITAS, C. J. & STREET, R. L. 1988 Non-linear transient phenomena in a complex recirculating flow: a numerical investigation. *Intl J. Numer. Meth. Fluids* **8** (7), 769–802.

GASKELL, P. H., GÜRCAN, F., SAVAGE, M. D. & THOMPSON, H. M. 1998 Stokes flow in a double-lid-driven cavity with free surface side walls. *Proc. Inst. Mech. Engrs* C **212** (5), 387–403.

GASKELL, P. H., SUMMERS, J. L., THOMPSON, H. M. & SAVAGE, M. D. 1996 Creeping flow analyses of free surface cavity flows. *Theor. Comput. Fluid Dyn.* **8** (6), 415–433.

GHIA, U., GHIA, K. N. & SHIN, C. T. 1982 High-*Re* solutions for incompressible flow using the Navier–Stokes equations and a multigrid method. *J. Comput. Phys.* **48**, 387–411.

GUCKENHEIMER, J. & HOLMES, P. 1983 *Nonlinear Oscillations, Dynamical Systems, and Bifurcations of Vector Fields, Applied Mathematical Sciences*, vol. 42. Springer.

HALLER, G. 2001 Distinguished material surfaces and coherent structures in three-dimensional fluid flows. *Physica* D **149** (4), 248–277.

HOFMANN, E. & KUHLMANN, H. C. 2011 Particle accumulation on periodic orbits by repeated free surface collisions. *Phys. Fluids* **23** (7), 072106.

HWANG, W. R., ANDERSON, P. D. & HULSEN, M. A. 2005 Chaotic advection in a cavity flow with rigid particles. *Phys. Fluids* **17**, 043602.

ISHII, K. & ADACHI, S. 2006 Numerical analysis of 3d vortical cavity flow. *Proc. Appl. Maths Mech.* **6**, 871–874.

ISHII, K. & IWATSU, R. 1990 Numerical simulation of the Lagrangian flow structure in a driven cavity. In *Topological Fluid Mechanics* (ed. H. K. Moffatt & A. Tsinober), pp. 54–63. Cambridge University Press.

ISHII, K., OTA, C. & ADACHI, S. 2012 Streamlines near a closed curve and chaotic streamlines in steady cavity flows. *Procedia IUTAM* **5**, 173–186.

IWATSU, R., ISHII, K., KAWAMURA, T., KUWAHARA, K. & HYUN, J. M. 1989 Numerical simulation of three-dimensional flow structure in a driven cavity. *Fluid Dyn. Res.* **5** (3), 173.

KROUJILINE, D. & STONE, H. A. 1999 Chaotic streamlines in steady bounded three-dimensional Stokes flows. *Physica* D **130**, 105–132.

KUHLMANN, H. C., ROMANÒ, F., WU, H. & ALBENSOEDER, S. 2016 Particle-motion attractors due to particle–boundary interaction in incompressible steady three-dimensional flows. In *The 20th Australasian Fluid Mechanics Conference* (ed. G. Ivey, T. Zhou, N. Jones & S. Draper), vol. 102, p. 449. Australasian Fluid Mechanics Society.

KUHLMANN, H. C., WANSCHURA, M. & RATH, H. J. 1997 Flow in two-sided lid-driven cavities: non-uniqueness, instabilities, and cellular structures. *J. Fluid Mech.* **336**, 267–299.

LEONG, C. W. & OTTINO, J. M. 1989 Experiments on mixing due to chaotic advection in a cavity. *J. Fluid Mech.* **209**, 463–499.

MOFFATT, H. K. 1964 Viscous and resistive eddies near a sharp corner. *J. Fluid Mech.* **18**, 1–18.

MUKIN, R. V. & KUHLMANN, H. C. 2013 Topology of hydrothermal waves in liquid bridges and dissipative structures of transported particles. *Phys. Rev.* E **88** (5), 053016.

MULDOON, F. H. & KUHLMANN, H. C. 2013 Coherent particulate structures by boundary interaction of small particles in confined periodic flows. *Physica* D **253**, 40–65.

MULDOON, F. H. & KUHLMANN, H. C. 2016 Origin of particle accumulation structures in liquid bridges: particle–boundary interactions versus inertia. *Phys. Fluids* **28**, 073305.

OTESKI, L., DUGUET, Y., PASTUR, L. & QUÉRÉ, P. L. 2015 Quasiperiodic routes to chaos in confined two-dimensional differential convection. *Phys. Rev.* E **92**, 043020.

OTTINO, J. M. 1989 *The Kinematics of Mixing: Stretching, Chaos, and Transport*, vol. 3. Cambridge University Press.

OTTINO, J. M. 1990 Mixing, chaotic advection, and turbulence. *Annu. Rev. Fluid Mech.* **22** (1), 207–254.

OTTINO, J. M. & KHAKHAR, D. V. 2000 Mixing and segregation of granular materials. *Annu. Rev. Fluid Mech.* **32**, 55–91.

PAI, S. A., PRAKASH, P. & PATNAIK, B. S. V. 2013 Numerical simulation of chaotic mixing in lid driven cavity: effect of passive plug. *Engng Appl. Comput. Fluid Mech.* **7** (3), 406–418.

PEYRET, R. 2013 *Spectral Methods for Incompressible Viscous Flow*, vol. 148. Springer.

PHILLIPS, T. N. & ROBERTS, G. W. 1993 The treatment of spurious pressure modes in spectral incompressible flow calculations. *J. Comput. Phys.* **105** (1), 150–164.

PIERREHUMBERT, R. T. 1986 Universal short-wave instability of two-dimensional eddies in an inviscid fluid. *Phys. Rev. Lett.* **57**, 2157–2159.

RAMANAN, N. & HOMSY, G. M. 1994 Linear stability of lid-driven cavity flow. *Phys. Fluids* **6**, 2690–2701.

RIECKE, H. & PAAP, H.-G. 1986 Stability and wave-vector restriction of axisymmetric Taylor vortex flow. *Phys. Rev.* A **33**, 547–553.

RUDMAN, M. 1998 Mixing and particle dispersion in the wavy vortex regime of Taylor–Couette flow. *Am. Inst. Chem. Engrs J.* **44**, 1015–1026.

SCHREIBER, R. & KELLER, H. B. 1983 Driven cavity flows by efficient numerical techniques. *J. Comput. Phys.* **49**, 310–333.

SCHWABE, D., MIZEV, A. I., UDHAYASANKAR, M. & TANAKA, S. 2007 Formation of dynamic particle accumulation structures in oscillatory thermocapillary flow in liquid bridges. *Phys. Fluids* **19**, 072102.

SHANKAR, P. N. & DESHPANDE, M. D. 2000 Fluid mechanics in the driven cavity. *Annu. Rev. Fluid Mech.* **32** (1), 93–136.

SHILNIKOV, L. P. 1965 A case of the existence of a denumerable set of periodic motions. *Sov. Math. Dokl.* **6**, 163–166.

SOTIROPOULOS, F. & VENTIKOS, Y. 2001 The three-dimensional structure of confined swirling flows with vortex breakdown. *J. Fluid Mech.* **426**, 155–175.

SOTIROPOULOS, F., VENTIKOS, Y. & LACKEY, T. C. 2001 Chaotic advection in three-dimensional stationary vortex-breakdown bubbles: Šil'nikov's chaos and the devil's staircase. *J. Fluid Mech.* **444**, 257–297.

TIWARI, R. K. & DAS, M. K. 2007 Heat transfer augmentation in a two-sided lid-driven differentially heated square cavity utilizing nanofluids. *Intl J. Heat Mass Transfer* **50**, 2002–2018.

WALEFFE, F. 1990 On the three-dimensional instability of strained vortices. *Phys. Fluids* **2**, 76–80.

XU, B. & GILCHRIST, J. F. 2010 Shear migration and chaotic mixing of particle suspensions in a time-periodic lid-driven cavity. *Phys. Fluids* **22** (5), 053301.